In vitro reconstitution reveals membrane clustering and double-stranded RNA recruitment by the enteroviral AAA+ ATPase 2C

Kasturika Shankar[1,2,3,4], Marie N. Sorin[1,2,3,4], Oskar Skoglund[1,2,3,4], Selma Dahmane[1,2,3,4], Himanshu Sharma[1,2,3,4], Josy ter Beek[1,2,4], Louise Nenzén[1,2,3,4], Lars-Anders Carlson[1,2,3,4,*]

1. Department of Medical Biochemistry and Biophysics, Umeå University, Umeå, Sweden

2. Wallenberg Centre for Molecular Medicine, Umeå University, Umeå, Sweden

3. Laboratory for Molecular Infection Medicine Sweden (MIMS), Umeå University, Umeå, Sweden

4. Umeå Centre for Microbial Research (UCMR), Umeå University, Umeå, Sweden

*corresponding author: lars-anders.carlson@umu.se

Keywords: enterovirus, picornavirus, poliovirus, AAA+ ATPase, cryo-electron tomography, membrane, in vitro reconstitution, 2C

Abstract

Enteroviruses are a vast genus of positive-sense RNA viruses that cause diseases ranging from common cold to poliomyelitis and viral myocarditis. They encode a membrane-bound AAA+ ATPase, 2C, that has been suggested to serve several roles in virus replication, e.g. as an RNA helicase and capsid assembly factor. Here, we report the reconstitution of full-length, poliovirus 2C association with membranes. We show that a conserved glycine divides the N-terminal membrane-binding domain of 2C into two amphipathic helix regions, AH1 and AH2. AH2 is the main mediator of 2C oligomerization, and is sufficient for its membrane binding. AH1 is the main mediator of a novel function of 2C: clustering of membranes. Cryo-electron tomography reveal that several 2C copies mediate this function by localizing to vesicle-vesicle interfaces. 2C-mediated clustering is partially outcompeted by nucleic acids, suggesting a way by which 2C can switch from an early role in coalescing replication organelles with lipid droplets, to a later role where 2C assists RNA replication and particle assembly. 2C is sufficient to recruit RNA to membranes, with a preference for double-stranded RNA, which is the replicating form of the viral genome. Finally, the *in vitro* reconstitution revealed that full-length, membrane-bound 2C has weak RNA chaperoning activity, but no appreciable ATP-dependent helicase activity. Together, this study suggests two novel roles for 2C in membrane clustering and double-stranded RNA recruitment to membranes, and calls into question a role of 2C as an RNA helicase. The reconstitution of functional, 2C-decorated vesicles provides a platform for further biochemical studies into this protein and its roles in enterovirus replication.

Introduction

The *Enterovirus* genus (family: *Picornaviridae*) are positive-sense single-stranded RNA (+ssRNA) viruses, whose ~7.5kb genome is encapsidated in a 30 nm non-enveloped, icosahedral capsid [1, 2]. There are hundreds of known human enteroviruses, responsible for diseases like poliomyelitis (poliovirus, PV), viral myocarditis (Coxsackievirus B3, CVB3), common cold (Rhinoviruses, RVs) and hand, foot and mouth disease (e.g., Coxsackievirus A16 and Enterovirus 71, EV71) [3-5]. In addition, their high mutation rate and frequent recombinations mean that novel enteroviruses emerge regularly [6-8]. PV, which causes the paralytic disease poliomyelitis, has been a major focus of enterovirus research and worldwide vaccination efforts. Since the launch of the Global Polio Eradication Initiative in 1988, the number of poliomyelitis cases have reduced significantly, but it continues to haunt a few countries as an endemic disease [9, 10]. There is limited progress in the production of vaccines against the many non-polio enteroviruses that cause frequent outbreaks in different parts of the world [11]. Development of pan-enteroviral drugs that inhibit conserved steps of the replication cycle is thus of importance not only for the last phase of polio eradication, but also for minimizing the risk associated with future enterovirus outbreaks, as well as for treating chronic enterovirus infections [12-15].

Enterovirus genome replication is a highly conserved process requiring the formation of cytoplasmic replication organelles (ROs) [16-18]. The ROs are formed from extensively modified cytoplasmic membranes which are turned into an assembly line for viral RNA and virus particles [19, 20]. RO membranes are obtained from several cellular sources. Initially, they come from the disassembly of the Golgi apparatus as well as from utilization of cellular cholesterol [21, 22]. In addition, ROs are enriched by fatty acids from lipid droplets, through RO-LD contacts mediated by the viral protein 2C [23]. At later time points, induction of macro-autophagy (henceforth: autophagy) provides another source of RO membranes in the form of double-membrane vesicles [24-26]. The direct dependence of enterovirus RNA replication on membranes is supported e.g. by electron microscopy autoradiography, showing that newly synthesized RNA co-localizes with RO membranes [27]. Further, subcellular fractions active in viral RNA synthesis contain membranes, and their activity is inhibited if the membranes are disintegrated by detergents [28, 29]. How viral RNA, viral proteins, and host factors arrange spatially on the cytoplasmic face of RO membranes is not known.

The enterovirus genome has one major open reading frame which is translated as a single major polyprotein, with some enteroviruses also having a smaller accessory open reading frame [30]. The major polyprotein is subsequently cleaved into eleven individual proteins by the viral proteases 2A and 3C (Fig. 1A). The non-structural proteins, contained in polyprotein regions P2 and P3, encode functions necessary for RO formation and genome replication (Fig. 1A). Amongst these is the protein 2C, a conserved, multifunctional ATPase of the AAA+ superfamily [31-33]. 2C is essential for both RNA replication and virion assembly, but its precise roles in these processes are unknown [34-38]. 2C has a central ATPase domain followed by a Zn finger and a C-terminal α-helix which engages a hydrophobic pocket of another 2C monomer to aid its oligomerization [39-42] (Fig. 1A). ATP hydrolysis by 2C is stimulated by its oligomerization [41, 43], and by binding to single-stranded RNA [44]. Interestingly, even though homologous proteins from other viruses are helicases, most publications report that 2C only has ATP-independent RNA chaperoning activity, and little-to-no ATP-dependent RNA helicase activity[44, 45]. However, it must be noted that biochemical studies on 2C have to date been carried out in simplified systems, using e.g. truncated 2C constructs, fusion proteins, and/or omitting the membrane platform on which 2C is located during infection.

The conserved, N-terminal membrane-binding domain (MBD) of 2C is necessary for virus replication [46]. It has been suggested to contain an amphipathic helix, and has been shown to be necessary and sufficient for membrane association when overexpressed in cells [46-48]. The MBD has further been described to mediate the hexamerization of poliovirus 2C [43], while the C-terminal α-helix appears sufficient to mediate hexamerization of 2C from some other enteroviruses [40]. Due to the

84 hydrophobic nature of the MBD, full-length 2C tends to aggregate during purification, thus prohibiting
85 its use in biochemical experiments. This problem has typically been circumvented by working with a
86 truncated 2C construct lacking the MBD [39-41], or by using high concentrations of detergents [44].
87 Alternatively, fusing the N-terminus of full-length 2C to the large, hydrophilic maltose-binding protein
88 (MBP) has also been reported to result in a soluble protein [43]. While all of these studies have
89 uncovered important aspects of 2C's function, they were not able to address the mechanisms of its
90 membrane binding, nor its function as a full-length protein on a membrane.

91 Here, we biochemically reconstituted the binding of purified, full-length poliovirus 2C to synthetic
92 vesicles. We suggest that the MBD is in fact composed of two amphipathic helix segments, AH1 and
93 AH2, interrupted by an absolutely conserved glycine residue. Both AH1 and AH2 are necessary for
94 complete hexamerization of 2C, whereas AH2 is sufficient for its membrane localization. A novel
95 function for AH1 is identified in tethering membranes together, and we show that 2C's membrane
96 tethering can be partially outcompeted by nucleic acid. We show that 2C is sufficient to recruit and
97 retain RNA to membranes, and that it has a strong preference for retaining double-stranded RNA at a
98 membrane. Together, these findings provide a biochemical basis for several roles of 2C in enterovirus
99 replication, and establishes a more realistic biochemical system as a basis for further investigations.

100

101 **Results**

102 **The oligomerization state of 2C is controlled by its N-terminal, bipartite amphipathic helix**

103 The membrane-binding domain (MBD) of 2C (Fig. 1A) consists of residues ~1-40 and is suggested to
104 be an amphipathic helix [46-48], but details of its structure are not known. We took a computational
105 approach to studying the MBD across enteroviruses. A multiple sequence alignment revealed that
106 several hydrophobic residues (W4, L5, F8, G17, W20, I25, F28, I29, W31, L32 and I36), polar
107 residues (S3, K6, K7, K24, K27, and K35) and P38 are broadly conserved between enterovirus species
108 (Fig. 1B). We next studied the amphipathic nature of the 1-40 region by calculating its hydrophobic
109 moment (μH) in a sliding window of 18 residues. A high value for hydrophobic moment means that a
110 helix is amphipathic (i.e. that one side is more hydrophobic than the other). The calculation suggested
111 that the MBD may, in fact, consist of two separate amphipathic helices, with the space between the
112 amphipathic regions coinciding with the conserved residue G17 (Fig. 1C). The amphipathic nature of
113 these two regions was corroborated by a helical wheel plot (Fig.S1A). Since glycine is a helix breaker
114 residue, we hypothesized that G17 in fact divides the MBD into two amphipathic helices, AH1 and
115 AH2. AlphaFold2 [49] structure predictions of 2C(1-40) of several enteroviruses indeed suggested that
116 a kink at G17 is a conserved structural feature (Fig. 1D). In addition, the structure predictions indicate
117 that AH1 has a hydrophobic surface which is offset from AH2 [50] (Fig. S1B). Together, these data
118 suggest that the MBD of 2C consists of two amphipathic helices, AH1 and AH2, and we thus set out
119 to study their individual roles in the protein.

120 Recombinant full-length 2C has been reported to be insoluble in the absence of detergents unless its
121 N-terminus is fused to a solubility-enhancing tag [39, 44]. We thus purified the N-terminally
122 His_6MBP-tagged, full-length poliovirus 2C protein (residues 1-329) and its N-terminally truncated
123 variants 2C(ΔAH1) (residues 12-329), 2C(ΔMBD) (residues 41-329) and 2C(Δ115) (residues 116-
124 329) (Fig. 2A, B, Fig. S2). The two first constructs correspond to the truncation of AH1, and AH1-2,
125 respectively, whereas the third construct corresponds to a soluble fragment which has previously been
126 crystallized [39]. Full-length 2C is a hexamer [39, 41, 43, 51]. We wanted to study the individual
127 roles of the AH1 and AH2 regions in hexamer assembly. Notably, every N-terminal truncation led to a
128 gradual shift towards higher elution volumes in size exclusion chromatography (Fig. 2B), indicating
129 that every part of the MBD plays a role in 2C oligomerization. To further dissect the role of AH1 and
130 AH2, we determined the molecular mass distribution of full-length and truncated 2C constructs. Mass

131 photometry of MBP-2C and MBP-2C(ΔAH1) at 100 nM revealed presence of monomeric protein, but
132 also high-mass peaks (Fig. 2C,D). For the full-length protein, the high-mass peak closely corresponds
133 to a hexamer, whereas the 2C(ΔAH1) high-mass peak corresponds to a pentamer, or e.g. a mix of
134 hexamer and a smaller species. The shorter constructs 2C(41-329) and 2C(116-329) were stable in
135 solution even after removal of the MBP tag, and their masses were analyzed at 38 µM and 134 µM,
136 respectively, by size exclusion chromatography coupled to multi-angle light scattering (SEC-MALS).
137 The mass estimates throughout the predominant peak for two consecutive runs were 43 kDa and 52
138 kDa for 2C(41-329), i.e. a mass intermediate between monomer (at 32.8 kDa) and dimer (Fig. 2E),
139 possibly due to an equilibrium between the two states. The predominant peak for two SEC-MALS
140 runs for 2C(116-329) gave an estimated mass of 27 kDa and 22 kDa, consistent with the expected 23.8
141 kDa of a monomer (Fig. 2F). The MBP-fused versions of these constructs both had SEC-MALS mass
142 estimates corresponding to monomers (Fig. S3A-B).

143 Taken together, the conserved glycine 17 divides the MBD into two amphipathic helices, AH1 and
144 AH2, with offset hydrophobic faces. Both AH1 and AH2 are important for hexamerization of 2C in
145 solution, and the deletion of the entire MBD only leaves 2C with a weak propensity for dimerization.

146

147 **The AH2 region mediates charge-independent binding of 2C to membranes**

148 We next wanted to study the individual roles of AH1 and AH2 in 2C's membrane binding. To this
149 end, we reconstituted the process *in vitro* using synthetic liposomes, and the purified 2C constructs
150 described above. We devised an assay in which MBP-fused 2C is first mixed with small or large
151 unilamellar vesicles (SUVs and LUVs, respectively), after which TEV protease is added to cleave off
152 the MBP tag and allow 2C to bind the liposomes (Fig. 3A). The 2C-decorated liposomes are then
153 subjected to a flotation assay, in which the liposome-containing upper fraction and liposome-free
154 lower fraction are separated. 2C and liposomes are labelled with different fluorophores (ATTO488
155 maleimide conjugated to cysteines, and ATTO647N conjugated to DOPE, respectively), allowing
156 quantification of 2C and lipids in the fractions (Fig. 3A). The lipid fluorescence readings in the upper
157 fraction were consistent across all experiments, allowing for quantitative comparisons of the amount
158 of protein bound to liposomes (Fig. S4). We first used SUVs composed of net uncharged lipids: 75
159 mol% 1-palmitoyl-2-oleoyl-glycero-3-phosphocholine (POPC), 25 mol% 1-palmitoyl-2-oleoyl-sn-
160 glycero-3-phosphoethanolamine (POPE). The SUVs had an average size of ~30 nm as determined by
161 dynamic light scattering (DLS) (Fig. S5). The addition of MBP-2C and TEV to the SUVs led to the
162 formation of two distinct SUV bands in the upper fraction (Fig. 3B, Fig. S6A). 88±11% of full-length
163 2C were found in the upper fraction, with most protein in the uppermost of the two bands (Fig. S6B).
164 MBP-fused 2C was able to associate with SUVs to a similar degree as cleaved 2C, indicating that the
165 MBD is exposed, also in the MBP fusion protein. However, later experiments would show that
166 removal of the MBP tag was necessary for functional association of 2C with membranes. Upon
167 deletion of AH1, 81±16 % of 2C(ΔAH1) was still found in the upper fraction, whereas deletion of the
168 entire MBD (AH1-AH2) led to only 10±7.4 % of 2C(41-329) being found in the upper fraction (Fig.
169 3C). Thus, the AH2 region is the main mediator of 2C membrane association.

170 We then wished to study if 2C has a preference for a given membrane charge or curvature. In side-by-
171 side flotation experiments, we quantitated 2C binding to the POPC/POPE (net uncharged) SUVs
172 described above, and SUVs consisting of 50 mol% phosphatidyl serine (POPS, net charge -1). Full-
173 length 2C and 2C(ΔAH1) showed no preference for the negatively charged POPS, whereas the binding
174 of 2C(41-329) increased from 10±7.4 % to 38±7% when POPS was included in the SUVs (Fig. 3D).
175 To determine if 2C has a membrane curvature preference, we compared 2C binding to the sonicated
176 POPC/POPE SUVs, with an average size of ~50 nm, and larger (and hence lower-curvature) LUVs
177 with the same lipid composition and an average diameter of ~2500 nm. Full-length 2C and 2C(ΔAH1)
178 showed a slight decrease in the binding to the lower-curvature LUVs (Fig. 3E), but this decrease was

179 no longer significant after normalizing for the amount of lipid present in the top fraction (Fig. S4F).In
180 summary, these data show that the AH2 region mediates strong 2C membrane binding, which is
181 neither dependent on high membrane curvature nor on negatively charged lipids.

182

183 **2C mediates lipid clustering, which is enhanced by the AH1 region**

184 In virus-infected cells, 2C is present at contact sites of ROs and lipid droplets[23], and we suspected
185 that the high-density band of 2C-coated SUVs in our flotation experiments may be an *in vitro*
186 recapitulation of 2C-mediated lipid tethering (Fig. 3B, Fig. S6B). We used DLS to investigate lipid
187 clustering by 2C. As described above, the MBP tag was cleaved from 2C in the presence of SUVs.
188 After a 30 min incubation, the size distribution of the sample was measured using DLS. The sonicated
189 SUVs were around 40 nm in size, whereas the addition of TEV protease and 0.8 μM MBP-2C to these
190 SUVs led to the formation of vesicle clusters with an average diameter of ~1 μm (Fig. 4A). 2C(ΔAH1)
191 also clustered SUVs (Fig. 4A). Defining a liposome cluster as a particle with a diameter of >100 nm(
192 2.5 times the average SUV size), we compared the percentage of clusters in reactions containing
193 different concentrations of 2C and 2C(ΔAH1). Already at 0.8 μM protein – the concentration used for
194 the flotation assays – full-length 2C generated significantly more clusters than 2C(ΔAH1) (11.5±4.0%
195 and 4.6±1.7%, respectively, Fig. 4B). At 3 μM 2C, the difference was even more pronounced, with
196 47.0±13% of liposomes being present in clusters with 2C and 12±13% for 2C(ΔAH1) (Fig. 4B). To
197 characterize the 2C-mediated vesicle clusters at nanometer resolution, we then performed cryo-
198 electron tomography (cryo-ET) on the 3 μM reaction with full-length 2C. This allowed direct
199 visualization of how 2C tethers liposomes together to form larger clusters (Fig. 4C). Typically,
200 multiple 2C densities were present on the imaged SUVs, and they were mostly found at the interface
201 between SUVs (Fig. 4C). Taken together, 2C clusters liposomes *in vitro*, and the AH1 region is
202 necessary for effective clustering.

203 **Nucleic acid binding competes with 2C membrane clustering, and 2C preferentially recruits**
204 **double-stranded RNA to membranes**

205 The enterovirus genome is replicated on the cytoplasmic face of the RO membrane [19, 52]. Since 2C
206 is a AAA+ protein and a putative RNA helicase [33, 36, 42, 44, 45, 53-56], we wondered whether 2C
207 is sufficient to recruit and retain RNA at the membrane, and whether nucleic acid binding may affect
208 2C's lipid clustering activity. To address the second question, we repeated the lipid clustering
209 experiment using full-length 2C, in the presence of increasing concentrations of nucleic acid. It was
210 previously reported that both DNA and RNA bind at the same site on 2C, and that initial binding is
211 dependent on the phosphodiester backbone [44]. Hence, we used single-stranded DNA (ssDNA)
212 oligonucleotide and measured the amount of clustering using DLS (Fig. 5A). Upon increasing the
213 concentration of ssDNA there was a consistent decrease in the percentage of clustered lipids, albeit
214 only statistically significant at 100 μM ssDNA concentration (Fig. 5B). This indicates that nucleic acid
215 binding partially outcompetes the membrane tethering activity of 2C. To directly test the hypothesis
216 that 2C recruits RNA to the membrane, and to investigate if it possesses any selectivity, we devised an
217 alternative SUV flotation assay. In this assay, 2C was no longer fluorophore-labelled. Instead, a
218 fluorophore-labeled RNA (single-stranded or double-stranded) was added in the first step of the
219 flotation assay, allowing quantitation of the amount of RNA co-migrating with the SUVs (Fig. 5C,
220 Fig. S7). 2C was able to recruit both ssRNA and dsRNA to SUVs and retain it at the membrane
221 throughout the ultracentrifugation of the flotation experiment (Fig. 5D). At identical starting
222 concentrations, dsRNA was recruited significantly more than ssRNA (Fig. 5D). The recruitment was
223 strictly dependent on 2C having a free MDB since omission of TEV protease completely abrogated the
224 RNA recruitment (Fig. 5D). Taken together, 2C recruits and retains nucleic acid to membranes, with a
225 preference for dsRNA over ssRNA, and nucleic acid binding reduces 2C-mediated membrane
226 clustering.

227

228 **Membrane-bound, full-length 2C is an ATPase and an ATP-independent RNA chaperone**

229 Several studies have sought to determine whether 2C is an active RNA helicase, but they were
230 generally conducted with protein that was truncated and/or not membrane-associated. Having
231 reconstituted the binding of full-length 2C to membranes, and shown that it recruits RNA to
232 membranes, we set out to use this more realistic system to revisit the question of 2C's helicase
233 activity. We conducted an RNA helicase assay using 2C and 2C(41-329) in the presence of SUVs. The
234 MBP-fused proteins were incubated with a dsRNA with 5' overhang, and either with or without TEV
235 protease and in the presence or absence of ATP. The unwinding of dsRNA to ssRNA was monitored
236 on a native polyacrylamide gel (Fig. 6A). This revealed that the release of 2C's N terminus from MBP
237 y the TEV protease was absolutely required for any RNA unwinding activity (Fig. 6A-B). With the N
238 terminus released, both 2C and 2C(41-329) showed partial RNA unwinding activity in the absence of
239 ATP, indicative of ATP-independent RNA chaperoning activity (Fig. 6A-B). However, the addition of
240 Mg^{2+}-ATP did not lead to increased unwinding of the dsRNA as expected from an RNA helicase. In
241 fact, the presence of Mg^{2+}-ATP instead led to less conversion of dsRNA to ssRNA (Fig. 6A-B). This
242 was consistent between full-length and truncated 2C, and the same was also seen when a dsRNA with
243 3' overhang was used (Fig. 6C-D). In stark contrast, when the ATPase activity of 2C was measured
244 under similar conditions, only the full-length protein was found to have appreciable ATPase activity,
245 and this was independent of whether it was fused to MBP, or if there was a membrane present (Fig.
246 6E). Notably, this correlates with the conditions for hexamerization of 2C (Fig. 2) but not with the
247 conditions under which 2C displayed RNA chaperoning activity (Fig. 6E). In summary, membrane-
248 bound full length 2C is an active ATPase, but its RNA chaperoning activity is not ATP-dependent.
249 The ATPase activity appears to correlate with the hexamerization of 2C, whereas the ATP-dependent
250 RNA chaperoning activity correlates with the liberation of its N-terminus.

251

252 **AH1 contributes to viral RNA replication to a similar degree as the entire MBD**

253 The biochemical reconstitution allowed us to study the separate contributions of AH1 and AH2 to
254 processes such as membrane binding and membrane clustering. To investigate their relative
255 contribution to viral RNA replication in cells, we used poliovirus replicons where the capsid proteins
256 were replaced by Renilla luciferase. As opposed to the biochemical experiments, the 2C truncations in
257 replicons (Δ(2-11) and Δ(2-40)) retained the staring glycine of 2C since it is a core part of the viral
258 protease 3C cleavage site (Fig. 7A). 12 hours after transfecting replicon RNAs into cells, they were
259 harvested, and the luciferase signal was quantified. The luminescence from both the Δ(2-11) and Δ(2-
260 40) replicons was significantly reduced, by approximately two orders of magnitude for the replicon
261 containing unaltered, full-length 2C. Thus, although AH1 appeared to have more subtle roles in the
262 biochemical experiments (e.g. in vesicle clustering), it is indispensable for effective viral RNA
263 replication in cells.

264

265 **Discussion**

266 With fewer than 7,000 coding nucleotides, the *Enterovirus* genome can sustain a full viral replication
267 cycle by encoding multifunctional proteins, and by hijacking host-cell functions. A universally present
268 and highly conserved enteroviral protein is the AAA+ ATPase 2C, whose suggested roles range from
269 membrane remodeling to RNA helicase and capsid morphogenesis. The nature of 2C as an
270 oligomerizing, peripheral membrane protein has impeded biochemical studies, that have typically been
271 conducted on truncated protein not engaging a membrane. Here we described the *in vitro*
272 reconstitution of purified, full-length 2C's binding to membranes. We used this more realistic, yet

273 completely defined, system to investigate several functions of 2C. In summary, our findings are
274 consistent with the model shown in Fig. 8.

275 We showed that the N-terminal MBD is divided into two amphipathic helix segments, AH1 and AH2,
276 separated by a highly conserved glycine residue (Fig. 1C, Fig. S1). AH2 appears to be the main
277 mediator of 2C's hexamerization in solution (Fig. 2), and is sufficient for membrane binding (Fig. 3C).
278 Of note, removal of the N-terminal maltose-binding protein (MBP) tag was not necessary for 2C to
279 bind membranes in our assay, but it was strictly required for 2C to recruit RNA to membranes (Fig.
280 5D), and for its RNA chaperoning activity (Fig. 6A). Whereas the N-terminal MBP tag is an artificial
281 addition to aid purification of recombinant 2C, the fusion of 2C's N-terminus to another protein is, in
282 fact, relevant to infection. 2C is initially excised from the viral polyprotein in the form of the stable
283 precursor 2BC, in which the N terminus of 2C is still fused to the viral protein 2B [57]. Hence, our
284 finding that 2C only binds RNA after its N terminus is liberated may be indicative of what happens in
285 an infected cell when 2BC is processed to 2B and 2C.

286 Our study revealed a novel role for 2C in clustering vesicles, a role mediated by AH1 (Fig. 4). This
287 finding suggest a biochemical mechanism for the 2C-mediated recruitment of lipid droplets to
288 replication organelles (ROs)[23]. 2C-mediated membrane clustering may also be involved in
289 generating the tightly stacked membrane tubes that make up the ROs at early time points [20, 58].
290 Notably, the deletion of AH1 led to a stark reduction of poliovirus genome replication, similar in
291 effect to the deletion of the entire MBD (Fig. 7). This may indicate that the lipid-clustering activity of
292 2C is central to enterovirus replication, although it cannot be ruled out that AH1 deletion also affects
293 other aspects of the replication such as polyprotein processing. The decrease in 2C-mediated
294 membrane clustering seen with increasing nucleic acid concentration (Fig. 5A-B) suggests a balance
295 between 2C's role in membrane clustering at early time points, and a preferential role in RNA
296 replication and particle assembly at later time points (Fig. 8). In this context, the ability of 2C to bind
297 membranes independent of curvature and lipid species (Fig. 3D-E) fits its multitude of roles in binding
298 to different types of RO membranes and lipid droplets.

299 The localization of viral RNA replication to RO membranes is well established, but the molecular
300 mechanism behind the localization is poorly understood. An electrostatic interaction between the viral
301 polymerase 3D and anionic lipids may be part of the mechanism[59]. Here, we show that 2C is able to
302 recruit and retain RNA at membranes, with a selectivity for dsRNA (Fig. 5D). Long double-stranded
303 segments are not prevalent amongst cellular RNAs, but it is the form of the viral template RNA while
304 replicated. Thus, 2C could selectively localize viral template RNA to the ROs. On the other hand, full-
305 length, membrane-bound 2C had no ATP-dependent RNA helicase activity, and only weak ATP-
306 independent RNA chaperone activity (Fig. 6A-D). This is in line with most previous studies on
307 truncated and membrane-free 2C, and with structural models of the 2C hexamer indicating that its
308 central pore would be too narrow and have an incompatible electrostatic potential to support RNA
309 translocation [40, 41, 44]. The conditions for 2C ATPase activity were different from the conditions
310 that permitted RNA chaperoning: effective ATPase activity required the MBD, but did not require
311 removal of the N-terminal MBP tag (Fig. 6E). One possible interpretation of these data is that 2C
312 ATPase activity requires hexamerization, whereas its RNA binding, and its weak RNA chaperoning
313 activity, requires a free N-terminus. A recent study found that MBD-deleted 2C has RNA-stimulated
314 ATPase activity, which would be consistent with the above interpretation of our data if assuming that
315 RNA engagement restores hexamerization of 2C(41-329). The convergence of our work and previous
316 studies in suggesting that 2C is not a helicase can be interpreted in the light of the reported dsRNA-
317 unwinding activity of the polymerase 3D [60].

318 Taken together, our reconstitution of 2C membrane binding allowed us to shed light on several
319 functions of 2C: it is able to bind vesicles with no apparent preference for curvature and lipid
320 composition, it can cluster vesicles, and selectively recruit dsRNA to their surface without possessing
321 helicase activity. In spite of this, major questions remain unanswered about the role of 2C in

322 enterovirus RNA replication and particle assembly. Nothing is known about the supramolecular
323 arrangement of the RNA replication machinery on membranes, for instance how 2C, the polymerase
324 3D and host RNA-binding proteins such as PCBP1/2 are arranged [61]. Also, 2C is known to play a
325 role in capsid assembly and is suggested to be part of a "tether complex" enabling the RNA loading of
326 new capsids on RO membranes [19, 58], but biochemical mechanisms underlying this process are
327 largely unknown. The reconstitution of 2C-decorated vesicles presented here is a stepping stone
328 towards a more complete *in vitro* reconstitution of such complex processes.

329

330 **Materials and methods**

331 **Expression and purification of poliovirus 2C**

332 A codon-optimized synthetic gene corresponding to full-length 2C from poliovirus type 1 Mahoney
333 (GenBank: V01149.1) was inserted into 1M expression plasmid from Macrolab (University of
334 California, Berkeley, USA) with a TEV protease-cleavable, N-terminal His_6-MBP tag. The plasmid
335 was transformed to *E. coli* BL21(DE3) competent cells and grown overnight on LB-agar plates
336 containing 50ug/ml Kanamycin (KAN). A single colony was used to inoculate LB/KAN media, this
337 primary culture was grown for 5 hours. Then, a one-liter culture of LB/KAN was inoculated with 1ml
338 of the primary culture. The cells were grown at 37°C, induced at OD_{600}=2 by the addition of 0.5 mM
339 isopropyl-beta-D-thiogalacopyranoside, then incubated overnight at 25°C. Cells were collected by
340 centrifugation, and resuspended in lysis buffer (50 mM Tris, pH 8.5), 500 mM NaCl, 20 mM
341 Imidazole, 10% (v/v) glycerol, 36 µM NP40, 5 mM $MgCl_2$, 0.1 mM THP) containing protease
342 inhibitor cocktail (40 mM Phenylmethylsulfonyl fluoride, 1 mM Leupeptin and 200 mM Benzamidine
343 HCl) and DNase. The cells were lysed using a continuous flow cell disruptor (Constant Systems). The
344 lysate was cleared by centrifugation at 63,000*g at 4°C for 1 hour and the supernatant was loaded onto
345 Ni-NTA (nitrilotriacetic acid) resin and eluted with elution buffer (50 mM Tris (pH 8.5), 500 mM
346 NaCl, 250 mM Imidazole, 10% (v/v) glycerol, 36 µM NP40, 5mM $MgCl_2$, 0.1 mM THP). The protein
347 was then loaded onto a HiTrap Q HP Column (GE Healthcare) and eluted using a gradient from buffer
348 QA (50 mM Tris, pH 8.5), 50 mM NaCl, 10% (v/v) glycerol, 36 µM NP40, 5 mM $MgCl_2$, 0.1 mM
349 THP) and buffer QB (50 mM Tris (pH 8.5), 1 M NaCl, 10% (v/v) glycerol, 36 µM NP40, 5 mM
350 $MgCl_2$, 0.1 mM THP). The fractions containing the protein was loaded onto a 24 ml Superose 6
351 Increase 10/300 GL (Cytiva) that was equilibrated with SEC buffer (50 mM Tris-HCl (pH 7.4), 150
352 mM potassium acetate, and 0.1 mM THP). Purified 2C was then aliquoted, flash frozen with liquid N_2,
353 and stored at -80°C. All the other constructs of the protein were purified in a similar way.

354 To prepare 2C(41-329) and 2C(116-329) without His_6-MBP tag, the tagged proteins were diluted to
355 0.1mg/ml after the HiTrap Q HP column using buffer QA described above and the proteins were
356 cleaved at 4°C overnight by adding TEV protease in a molar ration TEV:2C of 1: 5 and 1:15 for
357 2C(41-329) and 2C(116-329), respectively. Uncleaved protein and His_6-MBP were removed by
358 incubating the mixture with NiNTA resin followed by passing of the protein over a 1ml MBPTrap
359 (Cytiva) column and then a HiTrap Heparin HP (Cytiva) using buffer QA and QB. The fractions
360 containing the protein were loaded onto a Superdex 75 Increase 10/300 GL (Cytiva) equilibrated with
361 SEC buffer. Purified cleaved 2C was aliquoted, flash frozen with liquid N_2, and stored at -80°C.

362 **Fluorophore labeling of proteins**

363 To label the proteins, after the HiTrap Q HP Column, the proteins were incubated with an equimolar
364 amount of Atto488 maleimide (Sigma-Aldrich) at 4°C overnight. Next day, excess dye was quenched
365 using 25 mM Dithiothreitol (DTT) and the proteins were loaded onto a Superose 6 Increase 10/300 GL
366 (Cytiva) column, pooled and snap frozen as described above for unlabeled protein. The labeling
367 efficiency was estimated by measuring the absorption of the labeled protein at 280 nm and at the
368 fluorophore absorption maximum. It was typically 0.5-1.1 fluorophores/2C monomer.

369 **SEC-MALS**

370 All the samples were run on an ÄKTA Pure (Cytiva) with a Superdex 200 Increase 10/300 GL
371 column, equilibrated in SEC buffer, coupled to a light scattering (Wyatt Treas II) and refractive index
372 (Wyatt Optilab T-Rex) detector. Bovine serum albumin (BSA) was used to calibrate the system. 150
373 to 500 µl (0.6 to 1 mg/ml) of protein was injected at a flow rate of 400 µl/min. Data were analyzed
374 using Astra software (version 7.2.2; Wyatt Technology).

375 **Mass photometry**

376 Proteins were diluted to 100 nM in 50 mM Tris pH 7.4 and applied to a glass coverslip and recorded
377 on Mass Photometer[62] (OneMP, Refeyn Ltd) for 60 seconds. The data were analyzed using
378 DiscoverMP (Refeyn Ltd) and the molecular weight was obtained by contrast comparison with known
379 mass standards measured on the same day and were repeated three times, and visualized as mean +/-
380 standard deviation.

381 **Multiple sequence alignment**

382 Multiple sequence alignment of amino acids 1-40 was performed on EV71 (GenBank: AAB39969.1),
383 CVB3 (GenBank: AFD33642.1), PV type 1 (MAHONEY STRAIN) (GenBank: V01148.1), EV D68
384 (GenBank: ALE66301.1), RV A2 STRAIN USA/2018/CA-RGDS-1062 (GenBank: MN228695.1) and
385 RV C15 (GenBank: ACZ67658.1) using Clustal Omega[63] with default parameters.

386 **Amphipathic helix prediction**

387 The physicochemical properties 2C amino acids 1-40 from EV71 (GenBank: AAB39969.1), CVB3
388 (GenBank: AFD33642.1), PV type 1 (Mahoney strain) (GenBank: V01148.1), EV D68 (GenBank:
389 ALE66301.1), RV A2 STRAIN USA/2018/CA-RGDS-1062 (GenBank: MN228695.1) and RV C15
390 (GenBank: ACZ67658.1) were determined using heliquest (https://heliquest.ipmc.cnrs.fr/) [64] using
391 alpha-helix as helix type and window size of one turn (18 residues). The mean amphipathic moment or
392 transverse hydrophobic moment (µH) was plotted against the amino acid at the center of the analysis
393 window.

394 **Structure predictions**

395 All structures were predicted using Alphafold 2 implemented in COLABFOLD
396 ((https://colab.research.google.com/github/sokrypton/ColabFold/blob/main/AlphaFold2.ipynb) [49]
397 with default settings. The cartoon representations were generated using CHIMERAX [50].

398 **Preparation of small unilamellar vesicles (SUVs)**

399 1-palmitoyl-2-oleoyl-sn-glycero-3-phospho-L-serine (POPS), 1-palmitoyl-2-oleoyl-sn-glycero-3-
400 phosphoethanolamine (POPE) and 1-palmitoyl-2-oleoyl-sn-glycero-3-phosphocholine (POPC) were
401 purchased from Avanti Polar lipids. Total 1 mg/ml of lipids containing POPC (25 mol %), POPE (25
402 mol %), POPS (25 mol %) or POPC (75 mol %), POPE (25 mol %), and 1, 2-Dioleoyl-sn-glycero-3-
403 phosphoethanolamine labeled with Atto 647N (0.1 mol %) was dried onto a borosilicate glass tube
404 wall with a nitrogen stream and kept overnight in vacuum desiccator for complete removal of solvents.
405 500 µl of SEC buffer was added into the mixture. The tube was then vortexed to resuspend the lipids
406 and then, kept in a water bath at 42°C for 15 min. Then, the lipids were transferred to an Eppendorf
407 tube for sonicating with a tip sonicator (10 seconds pulse, 20 seconds rest, and 20% amplitude) until a
408 clear solution was observed. Then, the tube was centrifuged at 21,000*g at 4°C for 20 min. Then, 300
409 µl of supernatant was carefully removed, and the quality of the preparation was checked using
410 dynamic light scattering as described below. SUVs were kept at 4°C until use, at most for 3 days.

411 **Preparation of large unilamellar vesicles (LUVs)**

412 Total 1 mg/ml of lipids containing POPC (75 mol %), POPE (25 mol %) and1, 2-Dioleoyl-sn-glycero-
413 3-phosphoethanolamine labeled with Atto 647N (0.1 mol %) was dried onto a borosilicate glass tube
414 wall with a nitrogen stream and kept overnight in vacuum desiccator. Then, 500 µl of SEC buffer was
415 added into the mixture. The tube was then vortexed to resuspend the lipids and to break the multi-
416 lamellar vesicles, the lipids were subjected to 12 freeze-thaw cycles by moving it between a 42°C
417 water bath and liquid nitrogen. Then, this solution was passed 21 times through an extrusion
418 membrane (Whatman Nuclepore) with pore size of 2 µm on a mini-extruder (Avanti Polar Lipids) to
419 get a clear solution comprising of LUVs. The quality of the preparation was checked using Dynamic
420 light scattering as described below. LUVs were kept at 4°C until use, at most for 3 days.

421 **Vesicle flotation assay**

422 A reaction mixture of 100 µl was prepared containing 0.8 µM Atto488 maleimide His_6MBP-2C, 1
423 mg/ml SUVs or LUVs and X µM TEV protease was incubated for 2 hours at room temperature. Then,
424 this reaction mixture was mixed with 500 µl of 48% (w/v) OptiPrep density gradient medium (Merck
425 (Sigma-Aldrich)) and this mixture was carefully placed at the bottom of an Open-Top Thin wall Ultra-
426 Clear Tube (Beckman Coulter) and was overlaid with 800 µl of 30% (w/v) OptiPrep followed by
427 another layer of 800 µl of 20% (w/v) OptiPrep and finally 2 ml of SEC buffer. The tubes were then
428 ultra-centrifuged at 364,000*g for 3 hours at 4°C. After centrifugation different fractions were
429 carefully taken out from the tubes and fluorescence was measured using Agilent BioTek Synergy
430 fluorimeter.

431 **Flotation assay with fluorescently labeled RNA**

432 All oligonucleotides used in this study are listed in Table 1. 100 µl of reaction mixture was prepared as
433 described above, except that unlabeled 2C was used, and a final concentration of 500 nM of single-
434 stranded 5' TET-labeled RNA(5'CCUCUAACCACAGUCUGAUC 3') (Eurofins Genomics) or
435 dsRNA (described below) was added. The flotation assay was performed as described above and the
436 TET fluorescence was measured. To prepare dsRNA, 10uM of 5' TET labelled RNA
437 (5'CCUCUAACCACAGUCUGAUC 3') was mixed with its 10uM unlabeled complementary strand
438 in a buffer containing 50mM HEPES pH7.2, 100mM KCl and RNase secure. The mixture was heated
439 to 95°C and then the temperature was decreased by 0.5°C /minute until 22°C. The annealed dsRNA
440 was then placed overnight at 4°C and then at -20°C until use. The extent of annealing was checked
441 using a 16% acrylamide non-denaturing RNA gel. A standard curve was prepared using fluorescence
442 reading for ssRNA and dsRNA and the extent of binding of RNA to 2C was quantified using this
443 standard curve.

444 **Dynamic light scattering**

445 100 µl of reaction mixture was prepared containing 0.8 µM or 3 µM 2C, 1 mg/ml SUVs, and TEV
446 protease was incubated for 30 min at room temperature. Then, this mixture was transferred into a
447 cuvette and the particle size was determined by dynamic light scattering using a Zetasizer Nano-ZS
448 (Malvern Instruments, Worcestershire, UK) at room temperature. To check the effect of ssDNA on
449 clustering, increasing concentration of ssDNA oligo (5' TGAATGCGGCTAATCCCAACCT 3')
450 (Eurofins Genomics) was added in to the mix containing TEV protease, 1 mg/ml SUVs followed by
451 addition of protein and the particle size was determined as described above.

452 **Sample preparation for cryo-electron tomography**

453 A reaction mixture of 100 µl was prepared containing 3 µM His_6MBP-2C, 1 mg/ml SUVs and 4 µM
454 TEV protease was incubated for 30 min at room temperature. 3 µl of this mixture was blotted on a
455 glow-discharged Quantifoil R 2/1 Copper 300 mesh grid (Electron Microscopy Sciences) and plunge-
456 frozen in liquid ethane using a Vitrobot plunge freezer (ThermoFisher Scientific) at 22°C, 80%
457 humidity, with blot force -20, blot time 2 seconds and wait time 40 seconds.

458 **Cryo-electron tomography data collection and processing**

459 Tomographic tilt series were collected using a Titan Krios (ThermoFisher Scientific) operated at 300
460 kV, with a 100 µm objective aperture, Selectris energy filter and Falcon 4i detector (ThermoFisher
461 Scientific). Tilt series were acquired in dose-symmetric mode, using SerialEM version 4. The
462 following parameters were used for acquisition: 26,000 x nominal magnification corresponding to a
463 specimen pixel size of 4.7 Å; defocus range of -3 µm to -8 µm, ± 63° tilt-range with tilt increment of
464 3°; total electron dose ~116 $e^-/Å^2$. At each tilt angle, the exposure was saved as an EER movie. The
465 EER files were converted to TIFF files using IMOD [65], gain-reference corrected, and motion
466 corrected using MotionCor2 [66]. The tilt series were then processed and aligned using IMOD[65].
467 CTF was estimated using CTFFIND4 [67] and corrected using phase flipping as implemented in
468 IMOD's CTFPHASEFLIP.

469 The isotropic resolution and signal-to noise ratio of the tomograms were improved using the de-
470 noising deep-learning software IsoNet [68]. The filtered tomograms were used for segmentation using
471 Amira (Thermo Fisher Scientific) for the representation of SUVs and 2C.

472 **Colorimetric ATPase assay**

473 Malachite Green Phosphate Assay Kit (MAK307, Sigma-Aldrich) was used for the colorimetric
474 ATPase assay. For the enzymatic reaction 1.2 µM of His_6MBP-2C (1-329) or (41-329), 2.9 µM TEV
475 protease, 0.5 mg/ml SUV (POPC (25 mol %), POPE (25 mol %) and 0.4 mM ATP was mixed in
476 buffer containing 40 mM HEPES pH7.5, 2 mM DTT and 12 mM NaCl and was incubated for 2 hours
477 at 37 °C. The samples were diluted 20 times and plated in a 96 well plate and mixed with 20 µl
478 working reagent supplied with the kit. The mixture was incubated at 37°C for 30 min after which the
479 absorbance was measured at 620 nm according to manufacturer's instructions. A standard curved was
480 prepared using the provided standard phosphate in same buffer as the reaction. This standard curve
481 was used to determine the phosphate liberated in the ATPase assay.

482

483 **Double-stranded RNA unwinding assay**

484 The single stranded RNA (ssRNA) oligos (Eurofins Genomics) were annealed in molar ratio 1:1.5 (28
485 nucleotide labeled oligomer (5' AAAAAAAAAAAACCAGGCGACAUCAGCG-FAM3'): 16
486 oligomer un-labeled (5'CGCUGAUGUCGCCUGG3')) in a buffer containing 10 mM HEPES-NaOH
487 (pH 7.2) and 10 mM KCl. This mix was heated to 95°C for 1 minute and then cooled down to 22°C at
488 the rate of 1°C per minute. The sample was then kept at 22°C for one hour. The thus prepared dsRNA
489 with 5' overhang was kept at 4°C overnight before freezing at -20°C. The dsRNA with 3' overhang
490 was made similarly using 28 nucleotide labeled oligomer (FAM-
491 5'CCAGGCGACAUCAGCGAAAAAAAAAAAA3') and mixing with 16 oligomer un-labeled
492 (5'CGCUGAUGUCGCCUGG3'). Chaperone activity assay was performed in reaction buffer
493 containing 40 mM HEPES pH7.5, 2 mM DTT and 15mM NaCl, 0.5 µl RNAse inhibitor, 0.8 mg/ml of
494 SUVs (POPC (25 mol %), POPE (25 mol %) (the SUVs were prepared using the reaction buffer), 1.2
495 µM MBP-2C , 3.8 µM of TEV protease, 40 nM dsRNA template, 800 nM ssRNA trap strand (28
496 nucleotide un-labeled oligomer). This mixture was incubated at 37°C for 20 min, followed by addition
497 of 3.5 mM magnesium-ATP to start the reaction. The reaction was incubated for 2 hours before adding
498 5 µl of quenching buffer consisting of 100 mM Tris pH 7.5, 0.1% bromophenol blue, 1% SDS, 50 mM
499 EDTA, and 50% glycerol. The samples were run on 16% native polyacrylamide gels for 2 hours at
500 100 V and scanned using an Amersham Typhoon fluorescence gel scanner. The gel scans were
501 quantified using ImageJ, measuring the intensity of the bands at the ssRNA position as defined by the
502 ssRNA control and subtracting the intensity of the dsRNA control as background.

503

504 **Luciferase assay**

505 The P2-P3 region from poliovirus type 1 Mahoney (GenBank: V01149.1) was inserted into a vector
506 containing *Renilla* luciferase reporter on the N-terminus. Truncated 2C versions (Δ2-11 and Δ2-40)
507 were also constructed. The first glycine residue of 2C was not truncated in order to preserve the 3C
508 protease cleavage site. The plasmids were linearized using ApaI restriction enzyme followed by *in*
509 *vitro* transcription using MEGAscript™ T7 Transcription Kit (Invitrogen) according to manufacturer's
510 protocol. The quality of the RNA was checked using 0.5% denaturing agarose gel. For transfection, 1
511 µg RNA was used and transfected in HeLa cells using TransIT®-mRNA Transfection Kit (mirusbio)
512 according to manufacturer's instruction. The cells were harvested for luciferase assay after incubation
513 at 37°C for 12 hrs. The same procedure was repeated for GFP-CVB3 replicon RNA which was used as
514 transfection control (negative control for luciferase signal). The cells were lysed using lysis buffer
515 supplied with Renilla Luciferase Assay Kit 2.0 (Biotium). 20 µl of cell lysate was mixed with 100 µl
516 of freshly prepared working solution and the luminescence was recorded using a TECAN
517 spectrophotometer.

518

519 **Graphs and statistical procedure**

520 Statistical significance tests were performed using student's T-test as implemented in GraphPad Prism
521 v10.0.1. Error bars represent standard deviation. P value style: ; ns: $p > 0.05$; ; *: $p < 0.05$; **: $p < 0.01$;
522 ***: $p < 0.001$; ****: $p < 0.0001$

523

524 **Data availability**

525 The cryo-electron tomogram shown in Fig. 4C has been deposited to the Electron Microscopy Data
526 Bank with accession code EMD-XXXXX.

527 **Acknowledgements**

528 We would like to thank Madeleine Ramstedt (Department of Chemistry, Umeå University) for the
529 introduction to the Zetasizer Malvern Nanoz used for DLS measurements and Mikael Lindberg
530 (Protein expertise platform, Umeå University, part of Protein Production Sweden) for cloning the
531 poliovirus replicons. Cryo-ET was performed at the Umeå Center for Electron Microscopy (UCEM) a
532 SciLifeLab National Cryo-EM facility part of the National Microscopy Infrastructure, NMI (VR-RFI
533 2016–00968). This project was funded by a Human Frontier Science Program Career Development
534 Award (CDA00047/2017 C) to LAC, a Kempe foundations postdoctoral fellowship to MNS, an
535 MSCA fellowship to HS ("MsInfection", grant agreement ID: 101033469), the Knut and Alice
536 Wallenberg Foundation (through the Wallenberg Center for Molecular Medicine Umeå), and the
537 Swedish research council (grants 2018–05851 and 2021–01145).

538

539 **Figures and Tables**

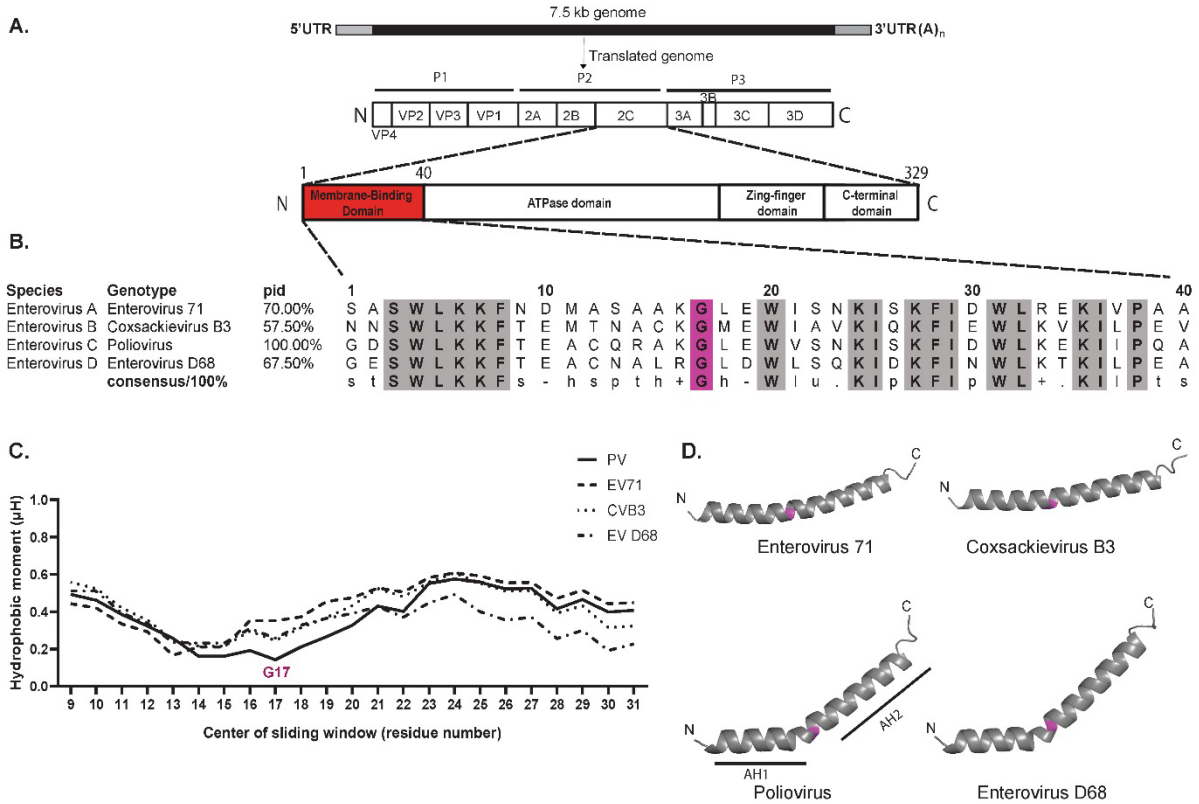

540

541 **Figure 1: The membrane-binding region of 2C consists of two amphipathic helix regions, separated by a**
542 **conserved glycine. (A)** Schematic representation of the *Enterovirus* genome, the translated polyprotein with
543 individual proteins marked, and the 2C protein with known domains marked. **(B)** Multiple sequence alignment of
544 the membrane-binding domain (MBD, residues 1-40) of 2C from representative genotypes of different
545 *Enterovirus* species. Conserved polar and hydrophobic residues are highlighted in grey (s: small residue, t: turn
546 like residue, h: hydrophobic residue, p: polar residue, l: aliphatic residue, +: positively charged residue, -:
547 negatively charged residue). The conserved glycine (number 17 in poliovirus 2C) is highlighted in pink. **(C)**
548 Hydrophobic moment (µH), a measure of the local amphiphilicity of a helix in a 18-residue sliding window, is
549 plotted for representative genotypes of different enterovirus species. The higher the µH value, the more an
550 amphipathic the helix at that position. The position of the conserved glycine 17 is marked. **(D)** Alphafold2
551 structure prediction of the MBD of 2C from representative genotypes of different enterovirus species. The
552 conserved glycine 17 is highlighted in pink separating AH1 and AH2.

553

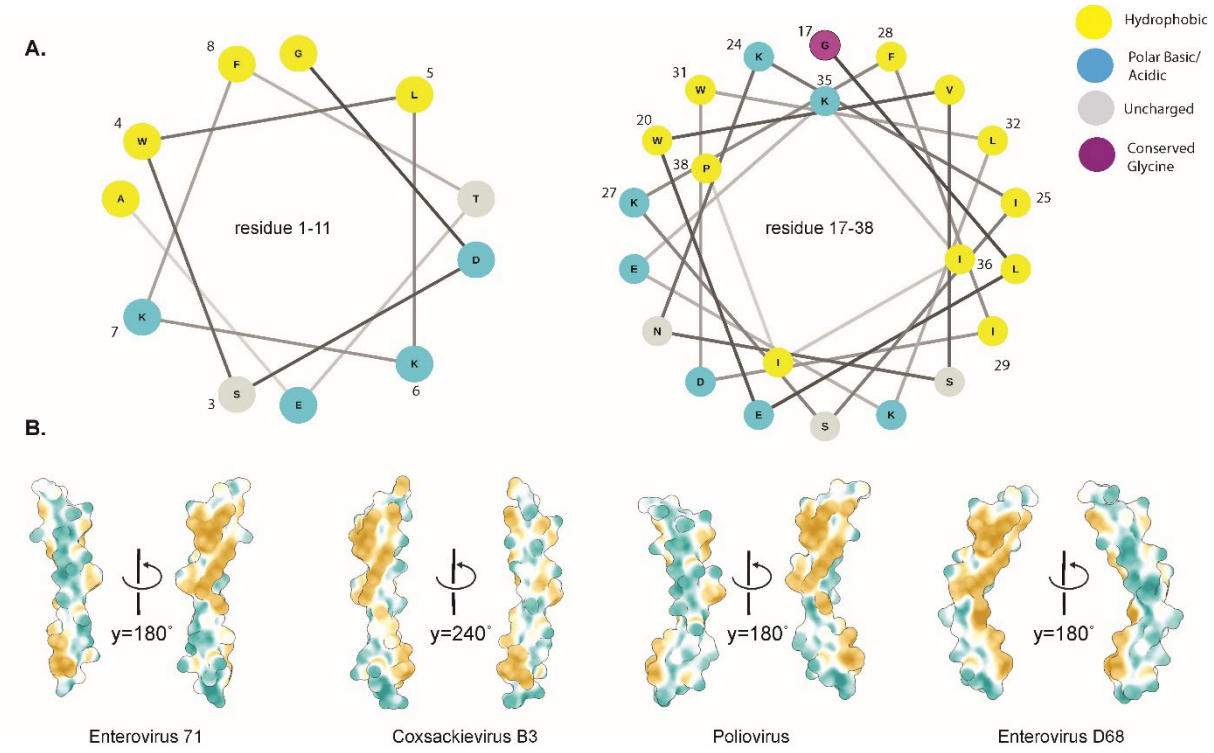

Figure S1: Amphipathic nature of the 2C membrane-binding domain. (A) Helical wheel of the AH1 and AH2 regions of poliovirus type 1 Mahoney 2C (GenBank: V01148.1) showing the distribution of hydrophobic and hydrophilic residues. Conserved residues are numbered. **(B)** Isosurface representations of Alphafold2-predicted structures of the MBD of different enterovirus genotypes showing the distribution of hydrophilic (blue) and hydrophobic (yellow) residues. For each structure prediction, two views related by the indicated rotation are shown.

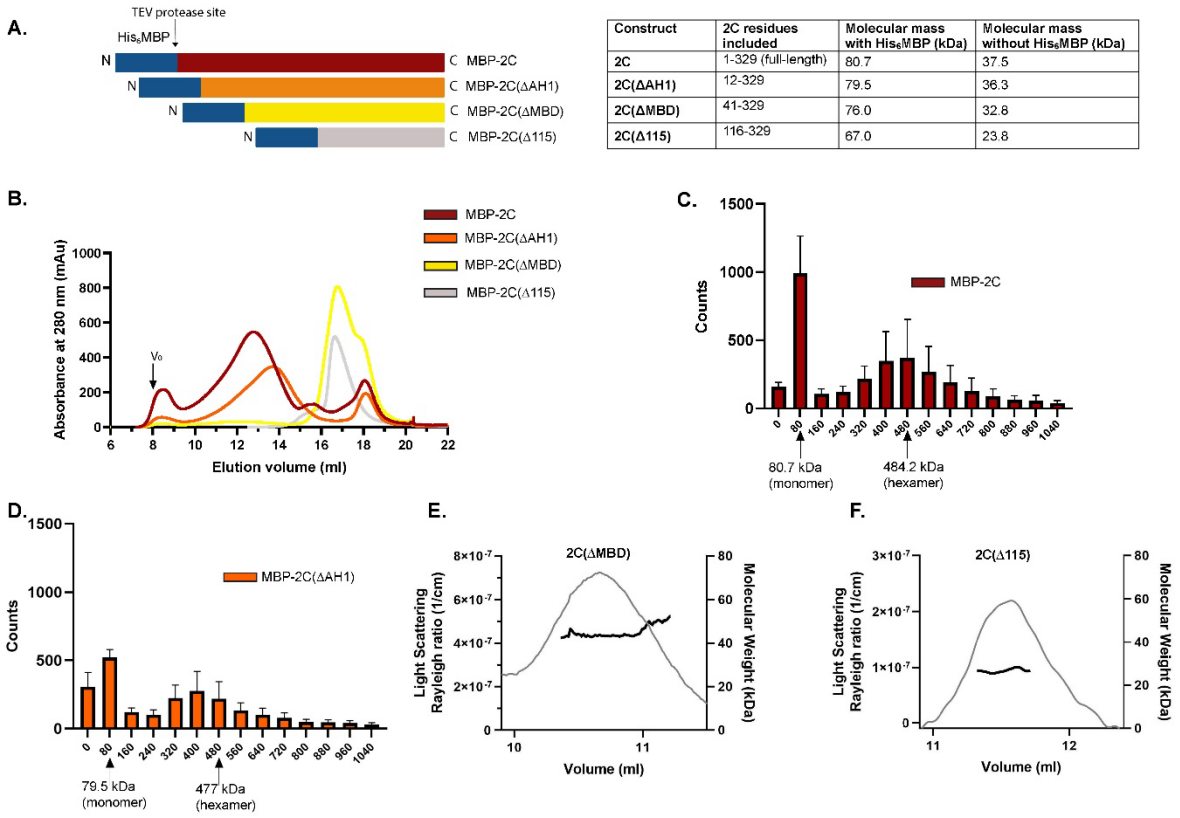

Construct	2C residues included	Molecular mass with His_6MBP (kDa)	Molecular mass without His_6MBP (kDa)
2C	1-329 (full-length)	80.7	37.5
2C(ΔAH1)	12-329	79.5	36.3
2C(ΔMBD)	41-329	76.0	32.8
2C(Δ115)	116-329	67.0	23.8

Figure 2: The membrane-binding domain regulates 2C oligomerization. (A) Schematic representation of all the His_6-MBP-(TEV) constructs used in the paper: full-length 2C, and N-terminally truncated versions: 2C(ΔAH1) corresponding to deletion of AH1, 2C(41-329) corresponding to deletion of AH1-2 (entire MBD), and 2C(116-329) corresponding to deletion of MBD and part of the ATPase domain (comparable to published crystal structure)[39]. **(B)** Elution profile of the constructs described in panel A on a Superose 6 Increase size-exclusion column. The peaks were centered at the following elution volumes: 12.5 ml for MBP-2C, 13.5 ml for MBP-2C(ΔAH1), 16.5 ml for MBP-2C(41-329), and 17.0 ml for MBP-2C(116-329). The column void volume is indicated with V_0. **(C-D)** Mass photometry data showing the molecular mass distribution at 100 nM concentration of C: MBP-2C(ΔAH1) and D: MBP-2C(ΔAH1). Error bars represent a standard deviation of three repeats of the experiment. **(E-F)** SEC-MALS data showing estimated molecular mass of MBP-free 2C(41-329) and 2C(116-329) at concentrations of 38 and 134 μM, respectively. Throughout the main elution peak, 2C(41-329) had an estimated mass of 43 and 52 kDa for two consecutive runs, whereas 2C(116-329) had an estimated mass of 22 and 27 kDa for two consecutive runs.

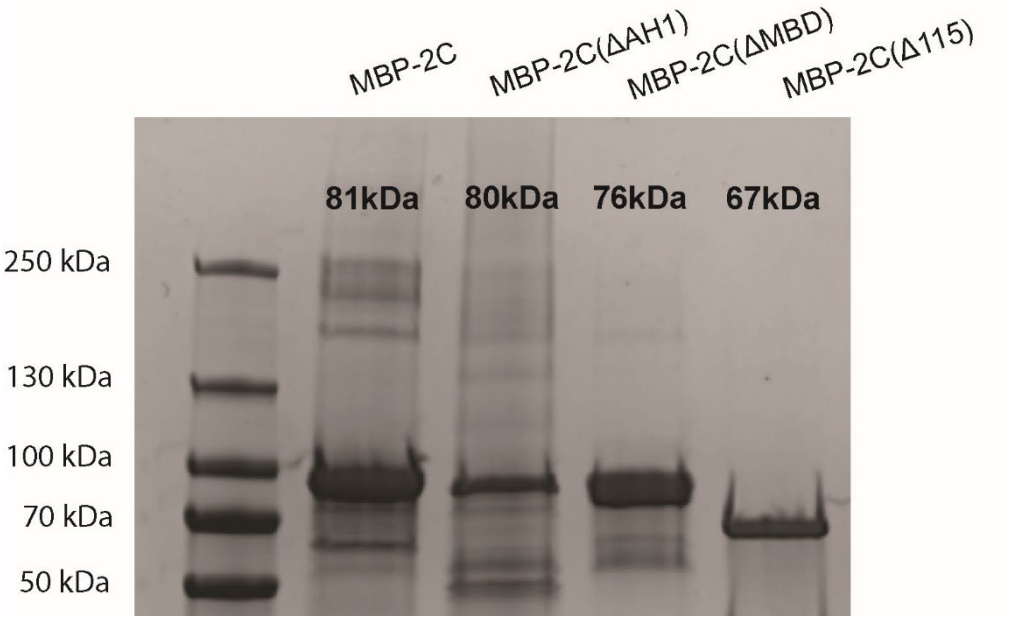

Figure S2: SDS PAGE gel showing different 2C constructs. lane 1: molecular mass ladder with masses indicated to its left. lane 2: His_6-MBP-(TEV)-full-length 2C, and N-terminally truncated versions: lane 3: His_6-MBP-(TEV)-2C(ΔAH1), lane 4: His_6-MBP-(TEV)-2C(41-329), and lane 5: His_6-MBP-(TEV)-2C(116-329).

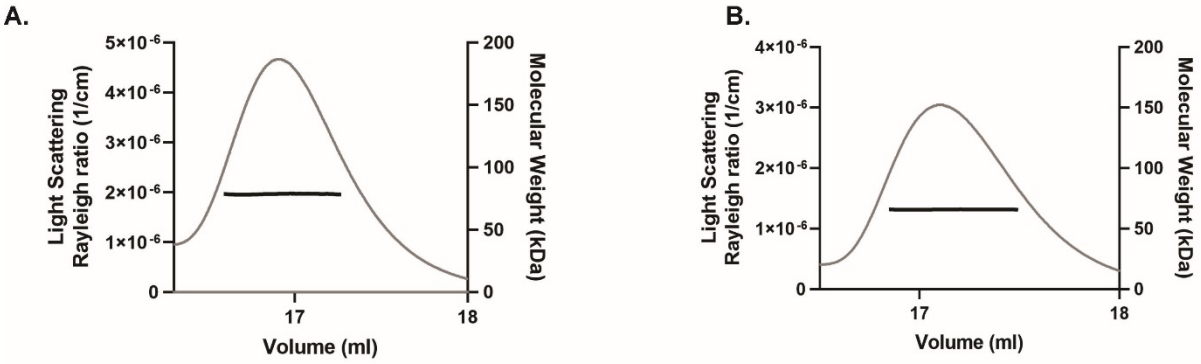

Figure S3: SEC-MALS mass analysis of MBP-fused truncated 2C constructs. SEC-MALS data showing estimated molecular mass throughout the main elution peak of (**A**) MBP-2C(41-329) and (**B**) MBP-2C(116-329) at concentrations of 38 and 134μM, respectively. The calculated masses are shown as a thick black line. MBP-2C(41-329) had an estimated mass of 78 kDa, whereas MBP-2C(116-329) had an estimated mass of 66 kDa.

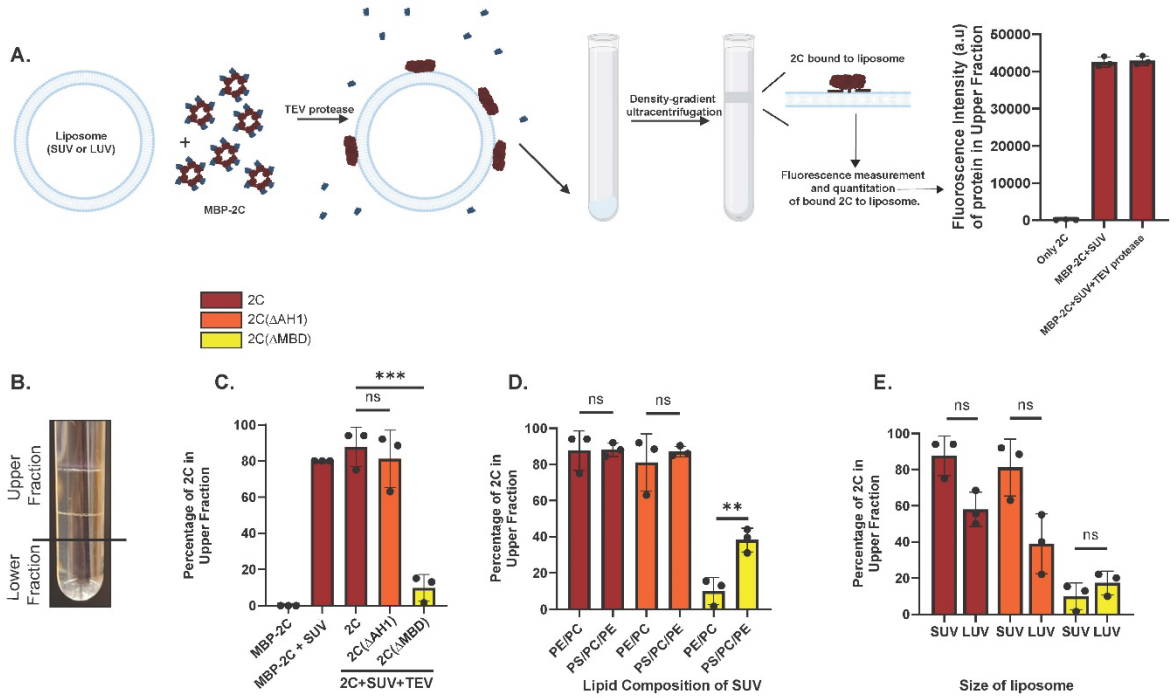

588

589 **Figure 3: The AH2 region is critical for 2C's membrane binding. (A)** Schematic representation of the
590 flotation assay used to quantify the membrane binding property of 2C. MBP-2C is fluorophore-labeled with
591 ATTO488 on exposed cysteines, which only exist in the 2C part of the fusion protein. Small unilamellar vesicles
592 (SUVs) or large unilamellar vesicles (LUVs) – collectively: liposomes – are labelled with DOPE-coupled
593 ATTO647N, thus having a distinct fluorescence signal from the protein. The MBP tag is cleaved from MBP-2C
594 using TEV protease in the presence of liposomes, allowing the liberated MBD to directly associate with the
595 liposomes. 2C-decorated liposomes are layered at the bottom of a density gradient and subjected to ultra-
596 centrifugation. The amount of liposomes present in the top fraction, and their bound 2C, is quantified in separate
597 channels of a fluorimeter. 2C hexamers are dark red, MBP blue. **(B)** Photograph of a representative centrifuge
598 tube after the flotation assay with 2C, showing two distinct lipid bands in the upper fraction. **(C)** Flotation assays
599 were conducted as shown in panel A, with SUVs composed of 75 mol% POPC and 25 mol% POPE, having an
600 average diameter of typically ~50 nm as measured by DLS. 2C fluorescence was measured separately in upper
601 and lower fractions, and the percentage present in the upper fraction is plotted for the different 2C constructs.
602 Error bars represent a standard deviation of three repeats of the experiment. Statistical significance by unpaired
603 two-tailed Student's t test; ns > 0.05; ***$p < 0.001$. **(D)** Flotation assay as in C, but with varying SUV lipid
604 composition. PE/PC: 25 mol% POPC, 75 mol% POPE. PE/PC/PS: 25 mol% POPC, 25 mol% POPE, 50 mol%
605 POPS. Error bars represent a standard deviation of three repeats of the experiment. Statistical significance by
606 unpaired two-tailed Student's t test; ns >0.05; **$p < 0.01$. **(E)** Flotation assay as in C, but with varying liposome
607 size. SUV: sonicated SUVs, ~50 nm diameter. LUV: extruded LUVs, ~2500 nm diameter. Error bars represent a
608 standard deviation of three repeats of the experiment. Statistical significance by unpaired two-tailed Student's t-
609 test; ns > 0.05.

610

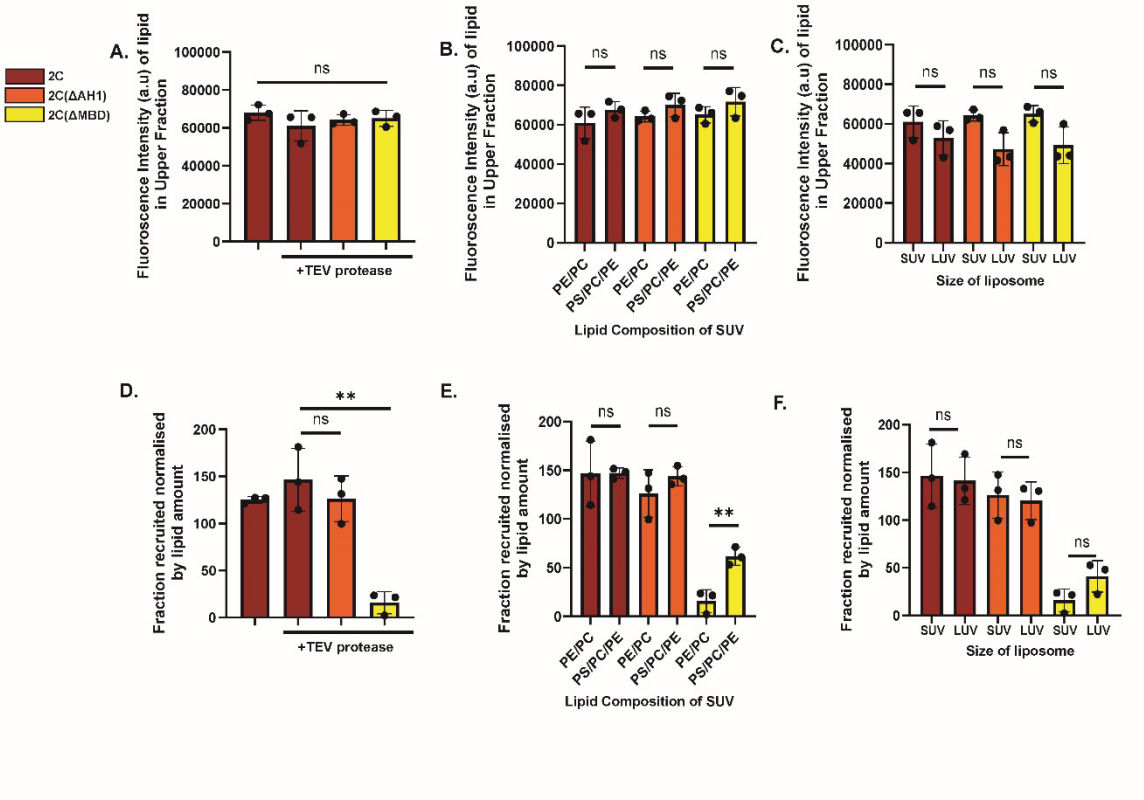

611

612 **Figure S4: Quantitation of lipid fluorescence in flotation experiments. (A-C)** Lipid fluorescence signal in the
613 upper fraction of the assays shown in Fig. 3C-E. Error bars represent a standard deviation of three repeats of the
614 experiment. Statistical significance by unpaired two-tailed Student's t test; ns > 0.05. (**D-E**) Fraction 2C
615 recruited to the upper fraction, normalized by amount of lipid in the upper fraction, for the assays shown in Fig.
616 3C-E. Error bars represent a standard deviation of three repeats of the experiment. Statistical significance by
617 unpaired two-tailed Student's t-test; ns > 0.05; **p < 0.01.

618

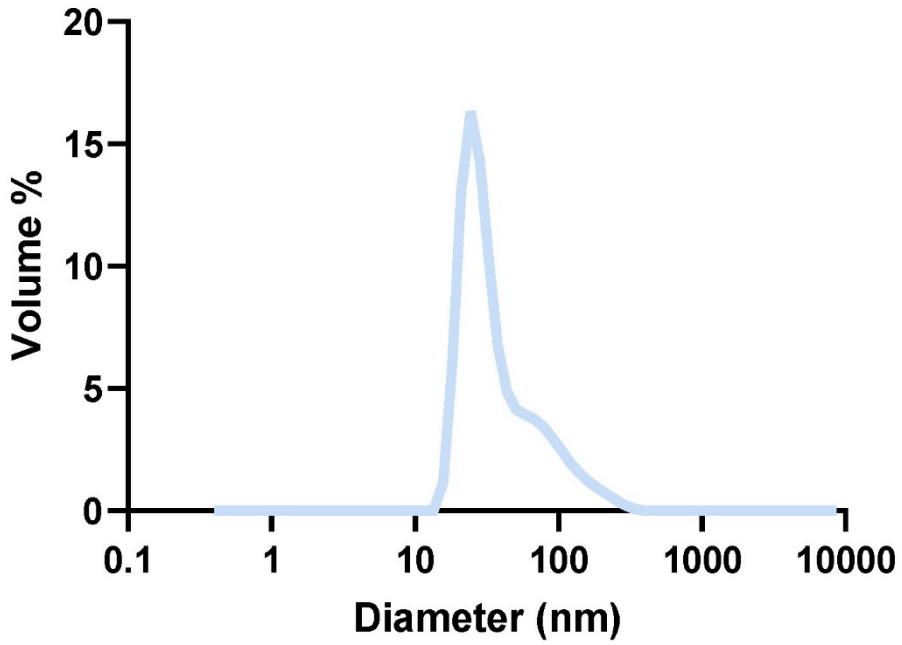

619

620 **Figure S5: Size distribution of SUVs.** Dynamic light scattering graph showing the size distribution of PE/PC
621 SUV (size distribution by volume). Average size of the SUVs was calculated to be 30 nm.

622

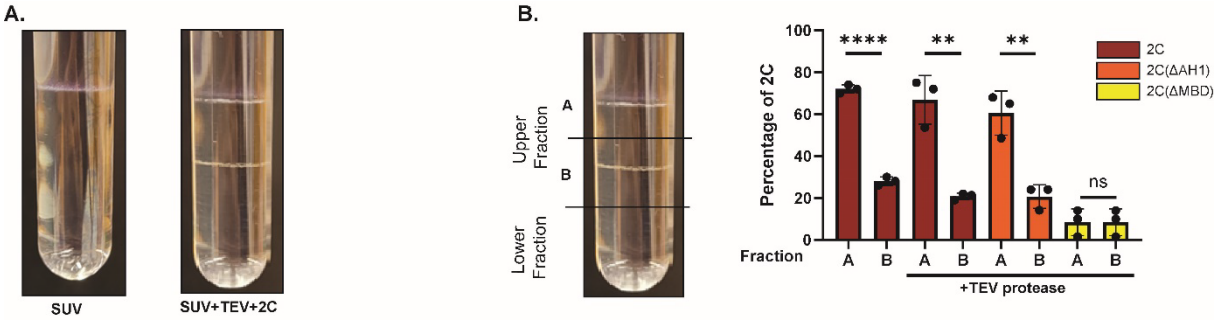

Figure S6: Two distinct lipid bands in the upper fraction in 2C flotation assays. (A) Photograph of representative centrifuge tubes after the flotation assay with SUVs only (single lipid band), and SUVs + TEV protease + MBP-2C (two lipid bands). **(B)** Photograph of centrifuge tube, indicating the upper fractions A, B, and the lower fraction. The percentage of the total 2C fluorescence in fractions A and B are shown. Error bars represent the standard deviation of three repeats of the experiment. Statistical significance by unpaired two-tailed Student's t-test; $^{**}p < 0.01$; $^{****}p < 0.0001$.

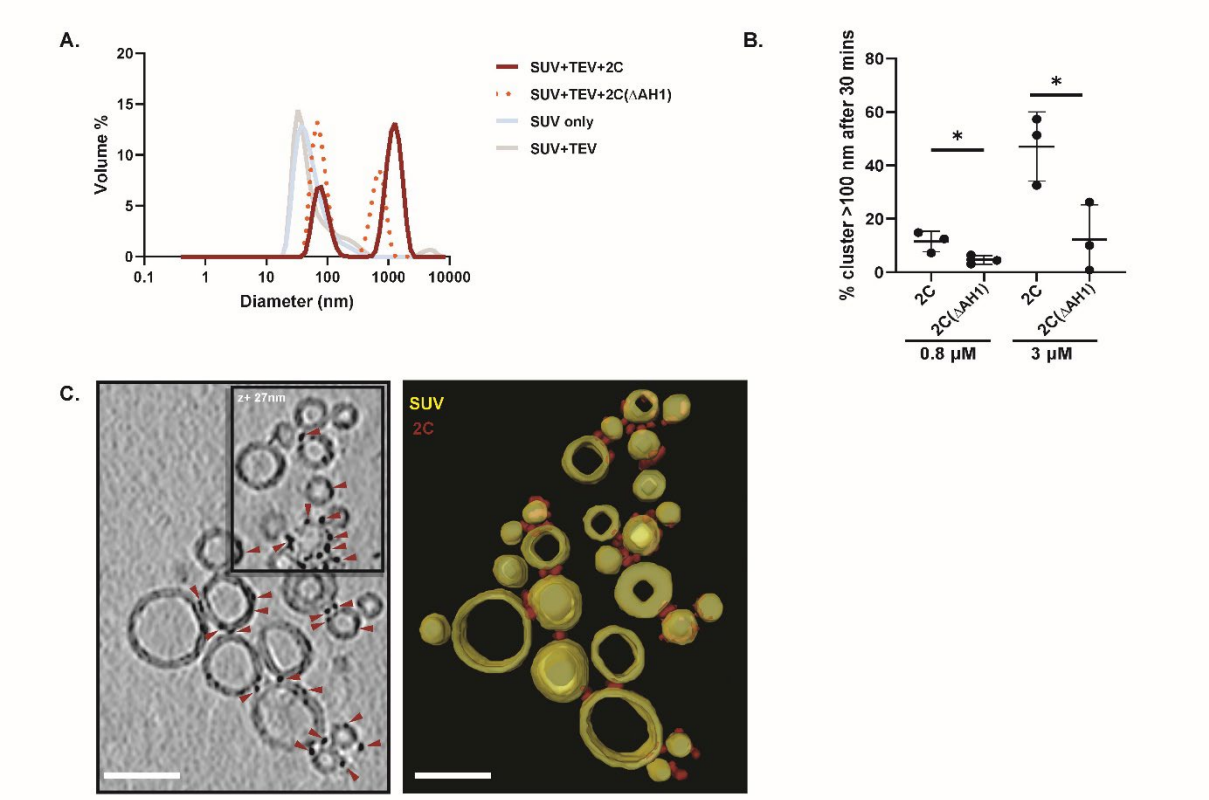

Figure 4: 2C has lipid clustering activity that is enhanced by the AH1 region. (A) Representative dynamic light scattering (DLS) graphs (size distribution by volume), showing the size distribution of the PE/PC SUV preparation, and appearance of additional peaks corresponding to vesicle clusters, 30 min after adding TEV protease and 3 μM MBP-2C (red solid line) or MBP-2C(ΔAH1) (orange dotted line) to SUVs (blue solid line). **(B)** Percentage of the total vesicle volume present in clusters (defined as particles with diameter > 100 nm), 30 min after adding TEV protease and 0.8 or 3 μM MBP-2C or MBP-2C(ΔAH1). Dots represent the average of triplicate measurements on the same SUV preparation, bars the average and error bars one standard deviation of the three independent replicates. Statistical significance by unpaired two-tailed Student's t-test; ns >0.05; **$p < 0.01$ **(C)** Computational slice through a representative cryo-electron tomogram of PE/PC SUVs, 30 min after adding TEV protease and 3 μM MBP-2C. Densities corresponding to 2C are pointed by red triangles. The right panel shows the corresponding three-dimensional segmentation showing 2C (red) and SUVs (yellow). Scale bar, 50 nm.

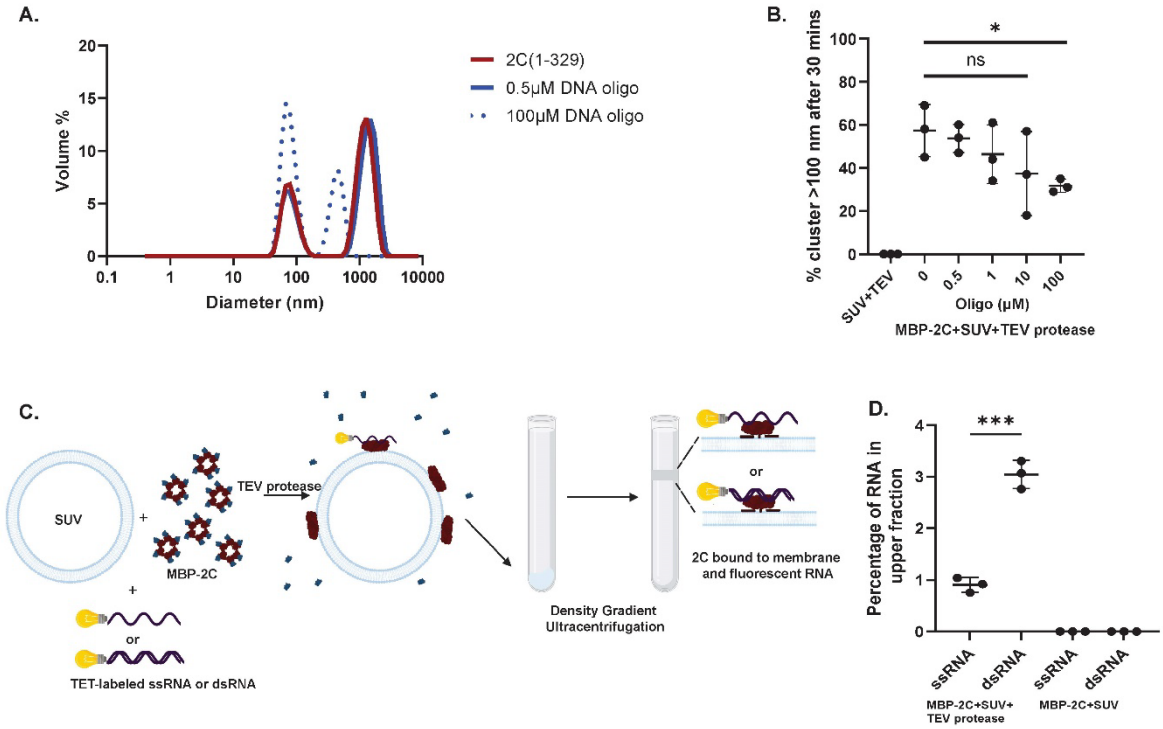

Figure 5: 2C preferentially recruits double-stranded RNA to membranes. (A) Representative DLS graphs (size distribution by volume), performed as for Fig. 4A with 3 μM 2C, but with the indicated concentrations of ssDNA oligonucleotide added. **(B)** Percentage of vesicle volume present as clusters (evaluated as for Fig. 4B), 30 min after addition of TEV protease, MBP-2C, and the indicated concentration of ssDNA oligonucleotide. Dots represent the average of triplicate measurements on the same SUV preparation, bars the average and error bars one standard deviation of the three independent replicates. Statistical significance by unpaired two-tailed Student's t test; ns >0.05; *$p < 0.05$. **(C)** Schematic representation of the flotation assay used to quantify RNA recruitment to membranes by 2C. The experiment is essentially performed as in Fig. 3A, except that MBP-2C is unlabeled, and the RNA (single-stranded, or annealed with a complementary strand for double-stranded) is labeled with TET fluorophore at its 5′ end (Fig. S8). Membrane-bound RNA is quantitated by measuring TET fluorescence in the upper fraction **(D)** Fluorescence from ssRNA and dsRNA in top fraction in the experiment outlined in (C). Dots represent the average of triplicate measurements on the same SUV preparation, bars the average and error bars one standard deviation of the three independent replicates. Statistical significance by unpaired two-tailed Student's t-test; ***$p < 0.001$.

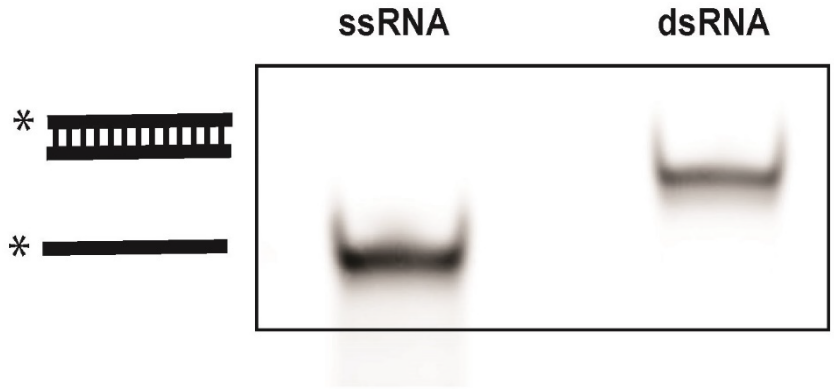

Figure S7: Characterization of fluorescent ssRNA and dsRNA. Fluorescence scan of non-denaturing polyacrylamide gel showing 5'TET-labelled ssRNA and 5'TET-labelled dsRNA.

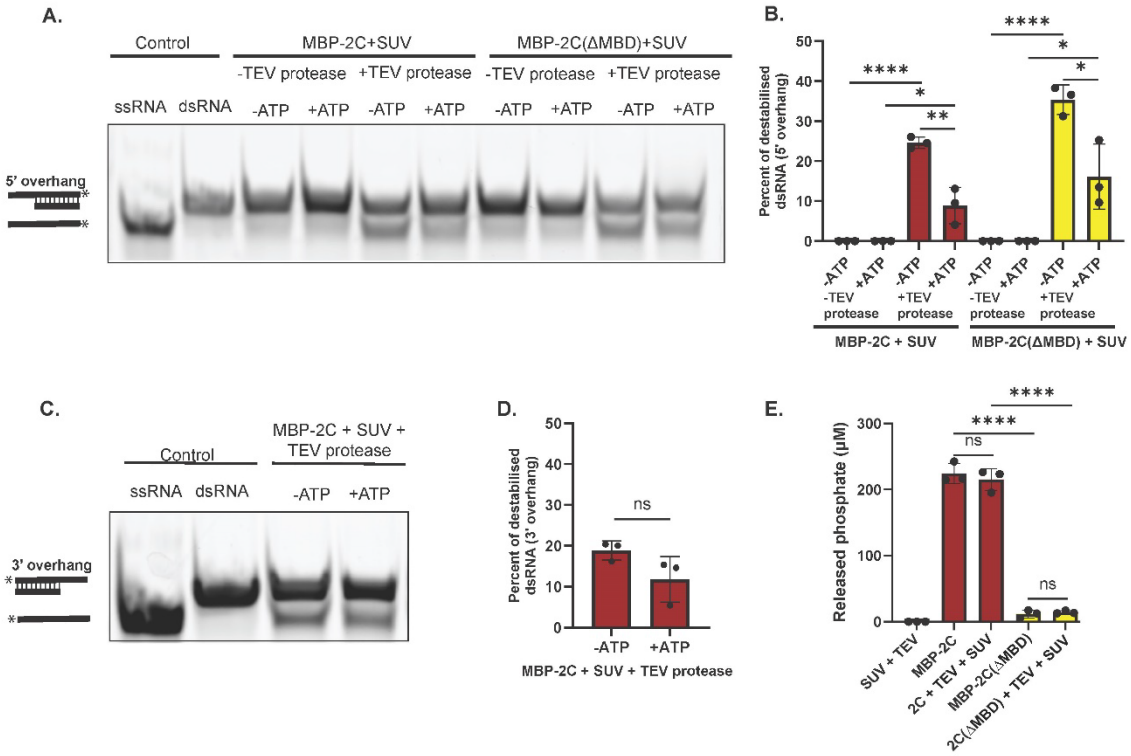

Figure 6: Membrane-bound, full-length 2C is an ATP-independent RNA chaperone. (A) Native polyacrylamide gel resolving dsRNA and ssRNA after a helicase assay. MBP-2C and MBP-2C(41-329) were incubated with dsRNA with a 5'overhang in the presence of SUVs, and presence or absence of TEV protease and Mg^{2+}-ATP. Lanes 1 and 2 from the left were loaded with ssRNA control and dsRNA substrate, respectively. The remaining lanes were loaded with RNA helicase reactions taken at the end of the two hour incubation, with proteins and reactants as indicated in the figure. A representative gel is shown, the experiment was performed in three independent replicates. **(B)** The percentage of total RNA signal (dsRNA and ssRNA) present as ssRNA is plotted for selected lanes of the gel in (A), and two independent replicates of the same experiment. Dots represent individual experiments, bars the average and error bars one standard deviation. The dsRNA lane was subtracted as background. Statistical significance by unpaired two-tailed Student's t-test; *$p < 0.05$; **$p < 0.01$; ****$p < 0.0001$. **(C)** Native polyacrylamide gel on a similar experiment to (A), but with a 3' overhang on the dsRNA. Lanes are labeled analogously to (A). **(D)** The percentage of total RNA signal (dsRNA and ssRNA) present as ssRNA is plotted for selected lanes of the gel in (C), and two independent replicates of the same experiment. Dots represent individual experiments, bars the average and error bars one standard deviation of the three independent replicates. The dsRNA lane was subtracted as background. Statistical significance by unpaired two-tailed Student's t test; ns > 0.05. **(E)** Colorimetric ATPase assay. MBP-2C and MBP-2C(41-329) were incubated with 0.4 mM ATP in the presence and absence of SUV+TEV protease. The amount of NTP hydrolyzed was determined and plotted. Dots represent individual experiments, bars the average and error bars one standard deviation. Statistical significance by unpaired two-tailed Student's t-test; ns > 0.05; ****$p < 0.0001$.

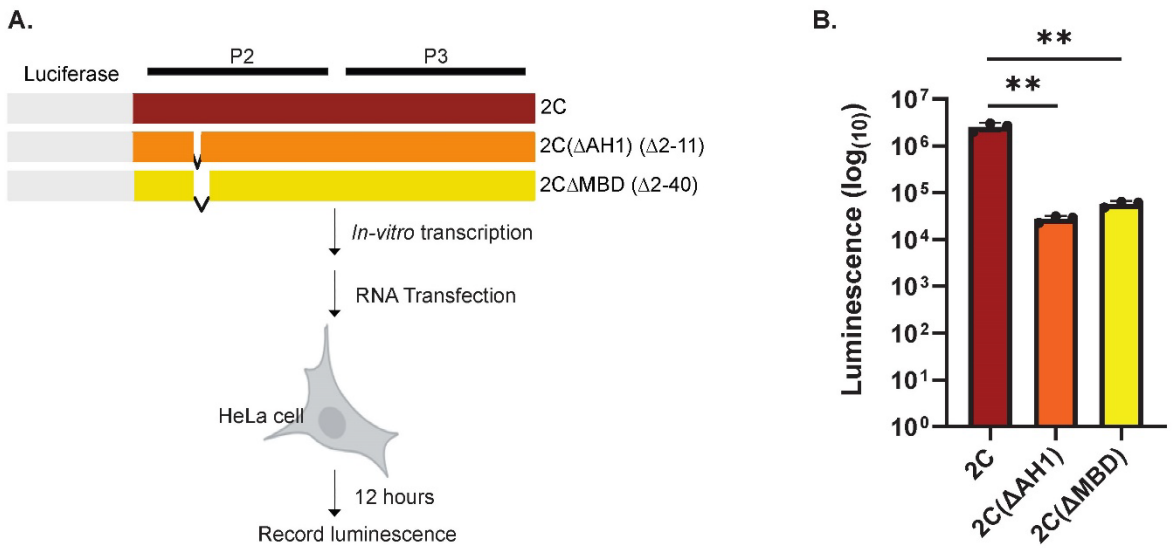

686

687 **Figure 7: Truncation of AH1 or the MBD drastically reduces poliovirus replication. (A)** Schematic
688 representation of poliovirus replicons and their use. The replicons contained Renilla luciferase in place of the
689 capsid region of the polyprotein, and the indicated deletions in the MBD of 2C. The first residue of 2C, glycine,
690 was kept in both deletions since it is a core part of the protease cleavage site. In vitro-transcribed RNAs from
691 these replicons were transfected into HeLa cells and luminescence was recorded 12 hours post-transfection. **(B)**
692 Luminescence recorded for cells transfected with different poliovirus replicons. Dots represent individual
693 experiments, bars the average, and error bars one standard deviation of the three independent replicates**.**
694 Statistical significance by unpaired two-tailed Student's t-test; $^{**}p < 0.01$.

695

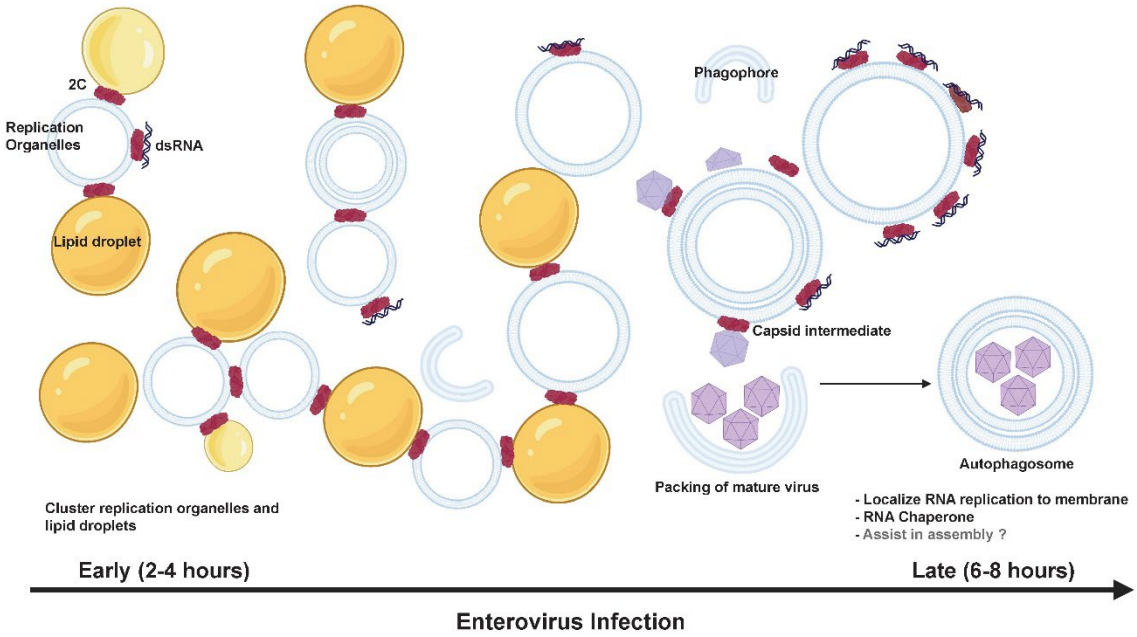

Figure 8: A model for the multiple roles of 2C in enterovirus replication. The model places the biochemical findings of this study into a suggested cellular context. At an early stage of infection, 2C serves to cluster replication organelle membranes and lipid droplets, while tethering the first viral dsRNA to the membrane. As the replication progresses, 2C is increasingly loaded with viral dsRNA and thus is a key component in localizing viral RNA replication to the replication organelle membranes. Our data suggest that 2C is an active ATPase but not and RNA helicase – a role which may be played by the polymerase 3D. Although not addressed in this study, the literature strongly suggests an additional role for 2C in capsid assembly and RNA loading, consistent with it being part of a "tethering complex" which tethers newly synthesized capsids to replication organelle membranes.

706 **Table 1: List of all the oligonucleotides used**

Oligo	Sequence 5'-3'	Type	Label
1	CCUCUAACCACAGUCUGAUC (20)	RNA	5' Tetrachlorofluorescein (TET)
2	GAUCAGACUGUGG UUAGAGG (20)	RNA	-
3	TGAATGCGGCTAATCCCAACCT (22)	DNA	-
4	AAAAAAAAAAAACCAGGCGACAUCAGCG (28)	RNA	3' Carboxyfluorescein (FAM)
5	CCAGGCGACAUCAGCGAAAAAAAAAAAA(28)	RNA	5' Carboxyfluorescein (FAM)
6	CGCUGAUGUCGCCUGG (16)	RNA	-

707

708

709

710 **Supplementary movie 1: Slices through cryo-electron tomogram showing vesicle clustering by 2C.** The
711 movie loops consecutive xy-planes of the cryo-electron tomogram shown in Fig. 4C.

712

713 **Supplementary movie 2. Surface model of cryo-electron tomogram showing vesicle clustering by 2C.** The
714 movie shows different views of the surface model of the tomogram shown in Fig. 4C.

715

716 **References**

717 1. Hyypia T, Hovi T, Knowles NJ, Stanway G. Classification of enteroviruses based on
718 molecular and biological properties. J Gen Virol. 1997;78 (Pt 1):1-11. doi: 10.1099/0022-1317-78-1-1.
719 PubMed PMID: 9010279.
720 2. Jiang P, Liu Y, Ma HC, Paul AV, Wimmer E. Picornavirus morphogenesis. Microbiol
721 Mol Biol Rev. 2014;78(3):418-37. Epub 2014/09/04. doi: 10.1128/MMBR.00012-14. PubMed PMID:
722 25184560; PubMed Central PMCID: PMCPMC4187686.
723 3. Adams MJ, Lefkowitz EJ, King AM, Bamford DH, Breitbart M, Davison AJ, et al.
724 Ratification vote on taxonomic proposals to the International Committee on Taxonomy of Viruses
725 (2015). Arch Virol. 2015;160(7):1837-50. doi: 10.1007/s00705-015-2425-z. PubMed PMID: 25913692.
726 4. Murphy OC, Messacar K, Benson L, Bove R, Carpenter JL, Crawford T, et al. Acute
727 flaccid myelitis: cause, diagnosis, and management. Lancet. 2021;397(10271):334-46. Epub 20201223.
728 doi: 10.1016/S0140-6736(20)32723-9. PubMed PMID: 33357469; PubMed Central PMCID:
729 PMCPMC7909727.
730 5. Holm-Hansen CC, Midgley SE, Fischer TK. Global emergence of enterovirus D68: a
731 systematic review. Lancet Infect Dis. 2016;16(5):e64-e75. Epub 20160224. doi: 10.1016/S1473-
732 3099(15)00543-5. PubMed PMID: 26929196.
733 6. Lukashev AN, Lashkevich VA, Ivanova OE, Koroleva GA, Hinkkanen AE, Ilonen J.
734 Recombination in circulating enteroviruses. J Virol. 2003;77(19):10423-31. doi:
735 10.1128/jvi.77.19.10423-10431.2003. PubMed PMID: 12970427; PubMed Central PMCID:
736 PMCPMC228507.
737 7. Chevaliez S, Szendroi A, Caro V, Balanant J, Guillot S, Berencsi G, et al. Molecular
738 comparison of echovirus 11 strains circulating in Europe during an epidemic of multisystem
739 hemorrhagic disease of infants indicates that evolution generally occurs by recombination. Virology.
740 2004;325(1):56-70. doi: 10.1016/j.virol.2004.04.026. PubMed PMID: 15231386.
741 8. Lukashev AN. Role of recombination in evolution of enteroviruses. Rev Med Virol.
742 2005;15(3):157-67. doi: 10.1002/rmv.457. PubMed PMID: 15578739.
743 9. Martini M, Orsini D. The fight against poliomyelitis through the history: past, present
744 and hopes for the future. Albert Sabin's missing Nobel and his "gift to all the world's children". Vaccine.
745 2022;40(47):6802-5. Epub 20221014. doi: 10.1016/j.vaccine.2022.09.088. PubMed PMID: 36244880.
746 10. Thompson KM, Lauring AS, Pollard AJ, Andino R, Bandyopadhyay AS, Berkley S, et
747 al. Polio eradication: Addressing the hurdles on the last mile. Cell. 2023;186(1):1-4. doi:
748 10.1016/j.cell.2022.12.021. PubMed PMID: 36608647.
749 11. Pons-Salort M, Parker EP, Grassly NC. The epidemiology of non-polio enteroviruses:
750 recent advances and outstanding questions. Curr Opin Infect Dis. 2015;28(5):479-87. doi:
751 10.1097/QCO.0000000000000187. PubMed PMID: 26203854; PubMed Central PMCID:
752 PMCPMC6624138.
753 12. Chapman NM, Kim KS. Persistent coxsackievirus infection: enterovirus persistence in
754 chronic myocarditis and dilated cardiomyopathy. Curr Top Microbiol Immunol. 2008;323:275-92. doi:
755 10.1007/978-3-540-75546-3_13. PubMed PMID: 18357775.
756 13. Anasir MI, Zarif F, Poh CL. Antivirals blocking entry of enteroviruses and therapeutic
757 potential. J Biomed Sci. 2021;28(1):10. Epub 20210115. doi: 10.1186/s12929-021-00708-8. PubMed
758 PMID: 33451326; PubMed Central PMCID: PMCPMC7811253.
759 14. Sun J, Yogarajah T, Lee RCH, Kaur P, Inoue M, Tan YW, et al. Drug repurposing of
760 pyrimidine analogs as potent antiviral compounds against human enterovirus A71 infection with
761 potential clinical applications. Sci Rep. 2020;10(1):8159. Epub 20200518. doi: 10.1038/s41598-020-
762 65152-4. PubMed PMID: 32424333; PubMed Central PMCID: PMCPMC7235037.
763 15. Kejriwal R, Evans T, Calabrese J, Swistak L, Alexandrescu L, Cohen M, et al.
764 Development of Enterovirus Antiviral Agents That Target the Viral 2C Protein. ChemMedChem.
765 2023;18(10):e202200541. Epub 20230310. doi: 10.1002/cmdc.202200541. PubMed PMID: 36792530.
766 16. Caliguiri LA, Tamm I. Membranous structures associated with translation and
767 transcription of poliovirus RNA. Science. 1969;166(3907):885-6. doi: 10.1126/science.166.3907.885.
768 PubMed PMID: 4310189.

769 17. Bienz K, Egger D, Rasser Y, Bossart W. Kinetics and location of poliovirus
770 macromolecular synthesis in correlation to virus-induced cytopathology. Virology. 1980;100(2):390-9.
771 doi: 10.1016/0042-6822(80)90530-9. PubMed PMID: 6243433.
772 18. Bienz K, Egger D, Rasser Y, Bossart W. Intracellular distribution of poliovirus proteins
773 and the induction of virus-specific cytoplasmic structures. Virology. 1983;131(1):39-48. doi:
774 10.1016/0042-6822(83)90531-7. PubMed PMID: 6316654.
775 19. Dahmane S, Kerviel A, Morado DR, Shankar K, Ahlman B, Lazarou M, et al. Membrane-
776 assisted assembly and selective secretory autophagy of enteroviruses. Nature communications.
777 2022;13(1):5986. Epub 2022/10/11. doi: 10.1038/s41467-022-33483-7. PubMed PMID: 36216808;
778 PubMed Central PMCID: PMCPMC9550805.
779 20. Limpens RW, van der Schaar HM, Kumar D, Koster AJ, Snijder EJ, van Kuppeveld FJ,
780 et al. The transformation of enterovirus replication structures: a three-dimensional study of single- and
781 double-membrane compartments. mBio. 2011;2(5). Epub 2011/10/06. doi: 10.1128/mBio.00166-11.
782 PubMed PMID: 21972238; PubMed Central PMCID: PMCPMC3187575.
783 21. Strating JR, van der Linden L, Albulescu L, Bigay J, Arita M, Delang L, et al.
784 Itraconazole inhibits enterovirus replication by targeting the oxysterol-binding protein. Cell Rep.
785 2015;10(4):600-15. Epub 20150129. doi: 10.1016/j.celrep.2014.12.054. PubMed PMID: 25640182;
786 PubMed Central PMCID: PMCPMC4383725.
787 22. Ilnytska O, Santiana M, Hsu NY, Du WL, Chen YH, Viktorova EG, et al. Enteroviruses
788 harness the cellular endocytic machinery to remodel the host cell cholesterol landscape for effective
789 viral replication. Cell Host Microbe. 2013;14(3):281-93. doi: 10.1016/j.chom.2013.08.002. PubMed
790 PMID: 24034614; PubMed Central PMCID: PMCPMC3802520.
791 23. Laufman O, Perrino J, Andino R. Viral Generated Inter-Organelle Contacts Redirect
792 Lipid Flux for Genome Replication. Cell. 2019;178(2):275-89 e16. Epub 2019/06/18. doi:
793 10.1016/j.cell.2019.05.030. PubMed PMID: 31204099; PubMed Central PMCID: PMCPMC7077330.
794 24. Schlegel A, Giddings TH, Jr., Ladinsky MS, Kirkegaard K. Cellular origin and
795 ultrastructure of membranes induced during poliovirus infection. J Virol. 1996;70(10):6576-88. doi:
796 10.1128/JVI.70.10.6576-6588.1996. PubMed PMID: 8794292; PubMed Central PMCID:
797 PMCPMC190698.
798 25. Hsu NY, Ilnytska O, Belov G, Santiana M, Chen YH, Takvorian PM, et al. Viral
799 reorganization of the secretory pathway generates distinct organelles for RNA replication. Cell.
800 2010;141(5):799-811. Epub 2010/06/01. doi: S0092-8674(10)00369-7 [pii]

801 10.1016/j.cell.2010.03.050. PubMed PMID: 20510927; PubMed Central PMCID: PMC2982146.
802 26. Miller S, Krijnse-Locker J. Modification of intracellular membrane structures for virus
803 replication. Nature reviews. 2008;6(5):363-74. Epub 2008/04/17. doi: nrmicro1890 [pii]

804 10.1038/nrmicro1890. PubMed PMID: 18414501.
805 27. Melia CE, van der Schaar HM, de Jong AWM, Lyoo HR, Snijder EJ, Koster AJ, et al.
806 The Origin, Dynamic Morphology, and PI4P-Independent Formation of Encephalomyocarditis Virus
807 Replication Organelles. mBio. 2018;9(2). Epub 20180417. doi: 10.1128/mBio.00420-18. PubMed
808 PMID: 29666283; PubMed Central PMCID: PMCPMC5904412.
809 28. Bienz K, Egger D, Pfister T, Troxler M. Structural and functional characterization of the
810 poliovirus replication complex. J Virol. 1992;66(5):2740-7. doi: 10.1128/JVI.66.5.2740-2747.1992.
811 PubMed PMID: 1313898; PubMed Central PMCID: PMCPMC241029.
812 29. Takeda N, Kuhn RJ, Yang CF, Takegami T, Wimmer E. Initiation of poliovirus plus-
813 strand RNA synthesis in a membrane complex of infected HeLa cells. J Virol. 1986;60(1):43-53. doi:
814 10.1128/JVI.60.1.43-53.1986. PubMed PMID: 3018300; PubMed Central PMCID: PMCPMC253900.
815 30. Guo H, Li Y, Liu G, Jiang Y, Shen S, Bi R, et al. A second open reading frame in human
816 enterovirus determines viral replication in intestinal epithelial cells. Nat Commun. 2019;10(1):4066.
817 Epub 20190906. doi: 10.1038/s41467-019-12040-9. PubMed PMID: 31492846; PubMed Central
818 PMCID: PMCPMC6731315.
819 31. Gorbalenya AE, Koonin EV, Wolf YI. A new superfamily of putative NTP-binding
820 domains encoded by genomes of small DNA and RNA viruses. FEBS Lett. 1990;262(1):145-8. doi:
821 10.1016/0014-5793(90)80175-i. PubMed PMID: 2156730.

822 32. Pfister T, Wimmer E. Characterization of the nucleoside triphosphatase activity of
823 poliovirus protein 2C reveals a mechanism by which guanidine inhibits poliovirus replication. J Biol
824 Chem. 1999;274(11):6992-7001. doi: 10.1074/jbc.274.11.6992. PubMed PMID: 10066753.
825 33. Teterina NL, Kean KM, Gorbalenya AE, Agol VI, Girard M. Analysis of the functional
826 significance of amino acid residues in the putative NTP-binding pattern of the poliovirus 2C protein. J
827 Gen Virol. 1992;73 (Pt 8):1977-86. doi: 10.1099/0022-1317-73-8-1977. PubMed PMID: 1322957.
828 34. Liu Y, Wang C, Mueller S, Paul AV, Wimmer E, Jiang P. Direct interaction between two
829 viral proteins, the nonstructural protein 2C and the capsid protein VP3, is required for enterovirus
830 morphogenesis. PLoS Pathog. 2010;6(8):e1001066. Epub 20100826. doi:
831 10.1371/journal.ppat.1001066. PubMed PMID: 20865167; PubMed Central PMCID:
832 PMCPMC2928791.
833 35. Vance LM, Moscufo N, Chow M, Heinz BA. Poliovirus 2C region functions during
834 encapsidation of viral RNA. J Virol. 1997;71(11):8759-65. Epub 1997/10/29. PubMed PMID: 9343235;
835 PubMed Central PMCID: PMCPMC192341.
836 36. Li JP, Baltimore D. Isolation of poliovirus 2C mutants defective in viral RNA synthesis.
837 J Virol. 1988;62(11):4016-21. doi: 10.1128/JVI.62.11.4016-4021.1988. PubMed PMID: 2845120;
838 PubMed Central PMCID: PMCPMC253830.
839 37. Pincus SE, Diamond DC, Emini EA, Wimmer E. Guanidine-selected mutants of
840 poliovirus: mapping of point mutations to polypeptide 2C. J Virol. 1986;57(2):638-46. doi:
841 10.1128/JVI.57.2.638-646.1986. PubMed PMID: 3003395; PubMed Central PMCID:
842 PMCPMC252779.
843 38. Tolskaya EA, Romanova LI, Kolesnikova MS, Gmyl AP, Gorbalenya AE, Agol VI.
844 Genetic studies on the poliovirus 2C protein, an NTPase. A plausible mechanism of guanidine effect on
845 the 2C function and evidence for the importance of 2C oligomerization. J Mol Biol. 1994;236(5):1310-
846 23. doi: 10.1016/0022-2836(94)90060-4. PubMed PMID: 8126722.
847 39. Guan H, Tian J, Zhang C, Qin B, Cui S. Crystal structure of a soluble fragment of
848 poliovirus 2CATPase. PLoS Pathog. 2018;14(9):e1007304. Epub 20180919. doi:
849 10.1371/journal.ppat.1007304. PubMed PMID: 30231078; PubMed Central PMCID:
850 PMCPMC6166989.
851 40. Guan H, Tian J, Qin B, Wojdyla JA, Wang B, Zhao Z, et al. Crystal structure of 2C
852 helicase from enterovirus 71. Sci Adv. 2017;3(4):e1602573. Epub 2017/05/17. doi:
853 10.1126/sciadv.1602573. PubMed PMID: 28508043; PubMed Central PMCID: PMCPMC5409451.
854 41. Hurdiss DL, El Kazzi P, Bauer L, Papageorgiou N, Ferron FP, Donselaar T, et al.
855 Fluoxetine targets an allosteric site in the enterovirus 2C AAA+ ATPase and stabilizes a ring-shaped
856 hexameric complex. Sci Adv. 2022;8(1):eabj7615. Epub 20220105. doi: 10.1126/sciadv.abj7615.
857 PubMed PMID: 34985963; PubMed Central PMCID: PMCPMC8730599.
858 42. Pfister T, Jones KW, Wimmer E. A cysteine-rich motif in poliovirus protein 2C(ATPase)
859 is involved in RNA replication and binds zinc in vitro. J Virol. 2000;74(1):334-43. doi:
860 10.1128/jvi.74.1.334-343.2000. PubMed PMID: 10590122; PubMed Central PMCID:
861 PMCPMC111544.
862 43. Adams P, Kandiah E, Effantin G, Steven AC, Ehrenfeld E. Poliovirus 2C protein forms
863 homo-oligomeric structures required for ATPase activity. J Biol Chem. 2009;284(33):22012-21. Epub
864 20090611. doi: 10.1074/jbc.M109.031807. PubMed PMID: 19520852; PubMed Central PMCID:
865 PMCPMC2755925.
866 44. Yeager C, Carter G, Gohara DW, Yennawar NH, Enemark EJ, Arnold JJ, et al.
867 Enteroviral 2C protein is an RNA-stimulated ATPase and uses a two-step mechanism for binding to
868 RNA and ATP. Nucleic Acids Res. 2022;50(20):11775-98. Epub 2022/11/19. doi:
869 10.1093/nar/gkac1054. PubMed PMID: 36399514; PubMed Central PMCID: PMCPMC9723501.
870 45. Xia H, Wang P, Wang GC, Yang J, Sun X, Wu W, et al. Human Enterovirus
871 Nonstructural Protein 2CATPase Functions as Both an RNA Helicase and ATP-Independent RNA
872 Chaperone. PLoS Pathog. 2015;11(7):e1005067. Epub 20150728. doi: 10.1371/journal.ppat.1005067.
873 PubMed PMID: 26218680; PubMed Central PMCID: PMCPMC4517893.
874 46. Paul AV, Molla A, Wimmer E. Studies of a putative amphipathic helix in the N-terminus
875 of poliovirus protein 2C. Virology. 1994;199(1):188-99. doi: 10.1006/viro.1994.1111. PubMed PMID:
876 8116242.

47. Echeverri AC, Dasgupta A. Amino terminal regions of poliovirus 2C protein mediate membrane binding. Virology. 1995;208(2):540-53. doi: 10.1006/viro.1995.1185. PubMed PMID: 7747426.
48. Echeverri A, Banerjee R, Dasgupta A. Amino-terminal region of poliovirus 2C protein is sufficient for membrane binding. Virus Res. 1998;54(2):217-23. doi: 10.1016/s0168-1702(98)00016-1. PubMed PMID: 9696129.
49. Jumper J, Evans R, Pritzel A, Green T, Figurnov M, Ronneberger O, et al. Highly accurate protein structure prediction with AlphaFold. Nature. 2021;596(7873):583-9. Epub 20210715. doi: 10.1038/s41586-021-03819-2. PubMed PMID: 34265844; PubMed Central PMCID: PMCPMC8371605.
50. Goddard TD, Huang CC, Meng EC, Pettersen EF, Couch GS, Morris JH, et al. UCSF ChimeraX: Meeting modern challenges in visualization and analysis. Protein Sci. 2018;27(1):14-25. Epub 2017/07/16. doi: 10.1002/pro.3235. PubMed PMID: 28710774; PubMed Central PMCID: PMCPMC5734306.
51. Papageorgiou N, Coutard B, Lantez V, Gautron E, Chauvet O, Baronti C, et al. The 2C putative helicase of echovirus 30 adopts a hexameric ring-shaped structure. Acta Crystallogr D Biol Crystallogr. 2010;66(Pt 10):1116-20. Epub 20100918. doi: 10.1107/S090744491002809X. PubMed PMID: 20944244.
52. Wolff G, Melia CE, Snijder EJ, Barcena M. Double-Membrane Vesicles as Platforms for Viral Replication. Trends Microbiol. 2020;28(12):1022-33. Epub 2020/06/17. doi: 10.1016/j.tim.2020.05.009. PubMed PMID: 32536523; PubMed Central PMCID: PMCPMC7289118.
53. Wang C, Jiang P, Sand C, Paul AV, Wimmer E. Alanine scanning of poliovirus 2CATPase reveals new genetic evidence that capsid protein/2CATPase interactions are essential for morphogenesis. J Virol. 2012;86(18):9964-75. Epub 20120703. doi: 10.1128/JVI.00914-12. PubMed PMID: 22761387; PubMed Central PMCID: PMCPMC3446611.
54. Rodriguez PL, Carrasco L. Poliovirus protein 2C contains two regions involved in RNA binding activity. J Biol Chem. 1995;270(17):10105-12. doi: 10.1074/jbc.270.17.10105. PubMed PMID: 7730315.
55. Rodriguez PL, Carrasco L. Poliovirus protein 2C has ATPase and GTPase activities. J Biol Chem. 1993;268(11):8105-10. PubMed PMID: 8385138.
56. Mirzayan C, Wimmer E. Genetic analysis of an NTP-binding motif in poliovirus polypeptide 2C. Virology. 1992;189(2):547-55. doi: 10.1016/0042-6822(92)90578-d. PubMed PMID: 1322588.
57. Cohen L, Kean KM, Girard M, Van der Werf S. Effects of P2 cleavage site mutations on poliovirus polyprotein processing. Virology. 1996;224(1):34-42. Epub 1996/10/01. doi: 10.1006/viro.1996.0504. PubMed PMID: 8862397.
58. Dahmane S, Shankar K, Carlson LA. A 3D view of how enteroviruses hijack autophagy. Autophagy. 2022:1-3. Epub 2022/12/07. doi: 10.1080/15548627.2022.2153572. PubMed PMID: 36471479.
59. Dubankova A, Humpolickova J, Klima M, Boura E. Negative charge and membrane-tethered viral 3B cooperate to recruit viral RNA dependent RNA polymerase 3D (pol). Scientific reports. 2017;7(1):17309. Epub 2017/12/13. doi: 10.1038/s41598-017-17621-6. PubMed PMID: 29230036; PubMed Central PMCID: PMCPMC5725453.
60. Cho MW, Richards OC, Dmitrieva TM, Agol V, Ehrenfeld E. RNA duplex unwinding activity of poliovirus RNA-dependent RNA polymerase 3Dpol. J Virol. 1993;67(6):3010-8. Epub 1993/06/01. doi: 10.1128/JVI.67.6.3010-3018.1993. PubMed PMID: 8388485; PubMed Central PMCID: PMCPMC237637.
61. Baggen J, Thibaut HJ, Strating J, van Kuppeveld FJM. The life cycle of non-polio enteroviruses and how to target it. Nature reviews. 2018;16(6):368-81. Epub 2018/04/08. doi: 10.1038/s41579-018-0005-4. PubMed PMID: 29626210.
62. Young G, Hundt N, Cole D, Fineberg A, Andrecka J, Tyler A, et al. Quantitative mass imaging of single biological macromolecules. Science. 2018;360(6387):423-7. doi: 10.1126/science.aar5839. PubMed PMID: 29700264; PubMed Central PMCID: PMCPMC6103225.
63. Sievers F, Wilm A, Dineen D, Gibson TJ, Karplus K, Li W, et al. Fast, scalable generation of high-quality protein multiple sequence alignments using Clustal Omega. Mol Syst Biol. 2011;7:539.

932 Epub 20111011. doi: 10.1038/msb.2011.75. PubMed PMID: 21988835; PubMed Central PMCID:
933 PMCPMC3261699.
934 64. Gautier R, Douguet D, Antonny B, Drin G. HELIQUEST: a web server to screen
935 sequences with specific alpha-helical properties. Bioinformatics. 2008;24(18):2101-2. Epub 20080728.
936 doi: 10.1093/bioinformatics/btn392. PubMed PMID: 18662927.
937 65. Mastronarde DN, Held SR. Automated tilt series alignment and tomographic
938 reconstruction in IMOD. J Struct Biol. 2017;197(2):102-13. Epub 20160719. doi:
939 10.1016/j.jsb.2016.07.011. PubMed PMID: 27444392; PubMed Central PMCID: PMCPMC5247408.
940 66. Zheng SQ, Palovcak E, Armache JP, Verba KA, Cheng Y, Agard DA. MotionCor2:
941 anisotropic correction of beam-induced motion for improved cryo-electron microscopy. Nat Methods.
942 2017;14(4):331-2. Epub 2017/03/03. doi: 10.1038/nmeth.4193. PubMed PMID: 28250466; PubMed
943 Central PMCID: PMCPMC5494038.
944 67. Rohou A, Grigorieff N. CTFFIND4: Fast and accurate defocus estimation from electron
945 micrographs. J Struct Biol. 2015;192(2):216-21. Epub 2015/08/19. doi: 10.1016/j.jsb.2015.08.008.
946 PubMed PMID: 26278980; PubMed Central PMCID: PMCPMC6760662.
947 68. Liu YT, Zhang H, Wang H, Tao CL, Bi GQ, Zhou ZH. Isotropic reconstruction for
948 electron tomography with deep learning. Nat Commun. 2022;13(1):6482. Epub 20221029. doi:
949 10.1038/s41467-022-33957-8. PubMed PMID: 36309499; PubMed Central PMCID:
950 PMCPMC9617606.

951